Medical Image Analysis 68 (2021) 101948

Contents lists available at ScienceDirect

Medical Image Analysis

journal homepage: www.elsevier.com/locate/media

Challenge report

Non-invasive estimation of relative pressure for intracardiac flows using virtual work-energy

David Marlevi[a], Maximilian Balmus[b], Andreas Hessenthaler[c], Federica Viola[d], Daniel Fovargue[b], Adelaide de Vecchi[b], Pablo Lamata[b], Nicholas S. Burris[e], Francis D. Pagani[e], Jan Engvall[d], Elazer R. Edelman[a], Tino Ebbers[d], David A. Nordsletten[b,f,*]

[a] *Institute for Medical Engineering and Science, Massachusetts Institute of Technology, 77 Massachusetts Avenue, Cambridge, MA 02139, USA*
[b] *School of Biomedical Engineering and Imaging Sciences, The Rayne Institute, King's College London, SE1 7EH, London, United Kingdom*
[c] *Institute for Modelling and Simulation of Biomechanical Systems, University of Stuttgart, Pfaffenwaldring 5a, 70569 Stuttgart, Germany*
[d] *Department of Medical and Health Sciences and Center for Medical Image Science and Visualization (CMIV), Linköping Unversity, SE-58185, Linköping, Sweden*
[e] *Department of Radiology, University of Michigan, 1500 E. Medical Center Drive, Ann Arbor, MI 48109, United States of America*
[f] *Department of Surgery and Biomedical Engineering, University of Michigan, 2800 Plymouth Rd, Ann Arbor, MI 48109, United States of America*

ARTICLE INFO

Article history:
Received 26 June 2020
Revised 10 December 2020
Accepted 11 December 2020
Available online 20 December 2020

Keywords:
Relative pressure
4D Flow MRI
Virtual work-energy
Cardiac hemodynamics
Dynamic domains
Fluid mechanics

ABSTRACT

Intracardiac blood flow is driven by differences in relative pressure, and assessing these is critical in understanding cardiac disease. Non-invasive image-based methods exist to assess relative pressure, however, the complex flow and dynamically moving fluid domain of the intracardiac space limits assessment. Recently, we proposed a method, νWERP, utilizing an auxiliary *virtual* field to probe relative pressure through complex, and previously inaccessible flow domains. Here we present an extension of νWERP for intracardiac flow assessments, solving the virtual field over sub-domains to effectively handle the dynamically shifting flow domain. The extended νWERP is validated in an *in-silico* benchmark problem, as well as in a patient-specific simulation model of the left heart, proving accurate over ranges of realistic image resolutions and noise levels, as well as superior to alternative approaches. Lastly, the extended νWERP is applied on clinically acquired 4D Flow MRI data, exhibiting realistic ventricular relative pressure patterns, as well as indicating signs of diastolic dysfunction in an exemplifying patient case. Summarized, the extended νWERP approach represents a directly applicable implementation for intracardiac flow assessments.

© 2020 The Authors. Published by Elsevier B.V.
This is an open access article under the CC BY license (http://creativecommons.org/licenses/by/4.0/)

1. Introduction

Cardiovascular diagnostics are driven by hemodynamic assessments (Richter and Edelman, 2006), and for the heart itself, evaluation of flow and pressure is part of clinical guidelines for a spectrum of cardiac disorders (Gersh et al., 2011; Baumgartner et al., 2017; Hunt et al., 2001). Intraventricular pressure gradients are attributed as the driving force behind both diastolic filling (Courtois et al., 1988) and systolic ejection (Pasipoularides et al., 1987), and variations in intraventricular pressure have been associated with a range of cardiovascular diseases. Disturbed intraventricular pressure gradients have been indicated in patients with left ventricular (LV) dyssynchrony (Arvidsson et al., 2018), reduction in early diastolic pressure gradients has been coupled to the loss of myocardial recoil in acute myocardial ischemia (Courtois et al., 1990), and decreased diastolic pressure gradients in patients with dilated cardiomyopathy have been linked to reduced diastolic suction (Yotti et al., 2005). Intraventricular pressure changes have also been used to differentiate heart failure patients with reduced vs. preserved ejection fraction (EF) (Londono-Hoyos et al., 2019), and clinical guidelines specify intraventricular pressure gradients as indicative of the severity of obstructive hypertrophic cardiomyopathy (Gersh et al., 2011; Geske et al., 2012). Quantitative and accurate

---

[*] Corresponding author.
E-mail addresses: marlevi@mit.edu (D. Marlevi), maximilian.balmus@kcl.ac.uk (M. Balmus), hessenthaler@imsb.uni-stuttgart.de (A. Hessenthaler), federica.viola@liu.se (F. Viola), daniel.fovargue@kcl.ac.uk (D. Fovargue), adelaide.de_vecchi@kcl.ac.uk (A.d. Vecchi), pablo.lamata@kcl.ac.uk (P. Lamata), nburris@med.umich.edu (N.S. Burris), fpagani@umich.edu (F.D. Pagani), jan.engvall@liu.se (J. Engvall), ere@mit.edu (E.R. Edelman), tino.ebbers@liu.se (T. Ebbers), nordslet@umich.com (D.A. Nordsletten).

https://doi.org/10.1016/j.media.2020.101948
1361-8415/© 2020 The Authors. Published by Elsevier B.V. This is an open access article under the CC BY license (http://creativecommons.org/licenses/by/4.0/)

assessment of intraventricular pressure behavior is thus an important diagnostic assessment tool for the management of cardiac disease.

To date, intracardiac catheterization provides real-time monitoring of intracardiac pressure (Courtois et al., 1988; Firstenberg et al., 2001), however, is inherently limited by its invasive nature and associated risks (Wyman et al., 1988; Vitiello et al., 1998). Instead, non-invasive imaging is routinely used to assess pressure differences *in-vivo*, where pressure is derived as a function of measured flow. Doppler echocardiography is by far the most commonly used modality for the evaluation of intracardiac hemodynamics, and measurements of peak velocities are linked to regional pressure drops using the simplified Bernoulli equation (Stamm and Martin, 1983). This method is part of clinical guidelines on the assessment valvular stenosis severity (Baumgartner et al., 2017), however, its assumption of unidirectional flow governed exclusively by advective motions limits its applicability within the intracardiac space. Modified Bernoulli-based methods, including expansions into an Euler momentum equation, have been proposed and applied on echocardiographic data of the heart (Firstenberg et al., 2000; Yotti et al., 2004; 2005), However discrepancies are still frequently reported against invasive catheter data (Feldman and Guerrero, 2016; Donati et al., 2017; Garcia et al., 2003), in part following from the way methods are utilized in clinical practice, assuming unidirectional flow as well as assigning integration paths along user-defined straight lines.

In comparison to conventional Doppler imaging, full-field mapping of cardiac flow is now achievable by 4D Flow Magnetic Resonance Imaging (4D Flow MRI) (Markl et al., 2012; Stankovic et al., 2014), and the technique has been used to map blood flow in both healthy and diseased intracardiac chambers (Ebbers et al., 2001; 2002; Eriksson et al., 2015; Töger et al., 2012; Vasanawala et al., 2015). The 4D nature of the technique allows for a complete fluid mechanical description of the acquired flow velocity data, which can be used to compute relative pressure. Both simplified and extended Bernoulli approaches have been attempted on 4D Flow MRI (Van Ooij et al., 2016; Allen et al., 2015; Ebbers et al., 2001; Jain et al., 2016), however they are all compromised in the heart by complex flow features obstructing the definition of an accurate center path along which to evaluate transient flow derivatives. Solution of a Pressure Poisson Equation (PPE) has also been utilized to map intraventricular pressure fields (Ebbers et al., 2002; Eriksson et al., 2015; Arvidsson et al., 2018), however the method has shown heavy dependence on accurate measurement of flow gradients and defined flow domain (Bertoglio et al., 2018; Donati et al., 2014). Quantification of turbulent flow by 4D Flow MRI has also been proposed as a way to more accurately estimate relative pressure (Gülan et al., 2017; Haraldsson et al., 2018; Marlevi et al., 2020), however such estimates have yet to be applied for intracardiac assessments.

Recently, a set of methods were introduced, all utilizing the concept of work-energy to derive relative pressure from acquired flow data. The Work-Energy Relative Pressure (WERP) method (Donati et al., 2015) represented an initial attempt using a direct work-energy form of the Navier-Stokes equations. This approach, however, was limited to peak flows as instabilities are observed during phases of low flow or in instances of complex bifurcating vasculatures. In subsequent work, the method was modified using a *virtual* work-energy form through IMRP (Bertoglio et al., 2018) and νWERP (Marlevi et al., 2019), which differ subtly in their treatment of some integral terms. In both cases, an auxiliary virtual field was introduced to overcome the theoretical limitations of WERP. νWERP was validated against invasive catheter data, where intra-aortic pressure gradients were derived in a clinical patient cohort with an estimation error below 1 mmHg. By incorporating turbulent energy dissipation, this virtual work-energy form was also successfully applied onto turbulence-driven flow fields (νWERP-t (Marlevi et al., 2020)), again with estimations validated against reference pressure measurements. However, whilst both promising and extending on previous presented methods, none of these virtual-work energy forms include implementations into time-varying intracardiac spaces, where the dynamically shifting flow domain complicates image-based assessment.

In this study we therefore present such an implementation, modifying νWERP to handle the dynamically changing flow domains of the intracardiac chambers. Based on the theoretical framework of the original νWERP, we here present the implementational variation required to handle dynamic flow domains, and further validate performance in a generic, *in-silico* benchmark problem. Further, we validate this implementation of νWERP in a patient-specific *in-silico* model of the left heart, mapping method behavior in a realistic flow scenario, as well as over ranges of realistic image noise. Lastly, we apply the method onto clinically acquired 4D Flow MRI data, assessing estimation output in a clinical control cohort as well as in a patient with diastolic dysfunction. In all cases, νWERP output is compared against alternative approaches, highlighting the benefits of the extended method, as well as providing theoretical and practical explanations to observed differences. All in all, the extension presented herein showcases the benefits of νWERP and presents an implementation directly applicable and viable for use in future cardiac flow assessments.

2. Methods

Starting with a short recapitulation of the principles of νWERP and the principles of virtual work-energy (Section 2.1), we outline the extension onto dynamic flow domains using both a generic Arbitrary Lagrangian-Eulerian approach (Section 2.2) as well as with a so called sub-domain approach (Section 2.3). We then provide details of the numerical implementation of the method on 4D flow data (Section 2.4). Continuing, we validate the method in a numerical benchmark problem (Section 2.5), as well as in a realistic patient-specific left heart model (Section 2.6), including both spatiotemporal and noise-sensitivity analyses. Lastly, we apply the method on clinically acquired 4D flow data, assessing output behavior in both healthy and diseased flow scenarios (Section 2.7).

2.1. Review of virtual work-energy relative pressure

The relationship between fluid velocity and pressure is well described by the Navier-Stokes equations, stating that

$$\rho \frac{\partial}{\partial t}\mathbf{v} + \rho \mathbf{v} \cdot \nabla \mathbf{v} - \mu \nabla^2 \mathbf{v} + \nabla p = 0, \tag{1}$$

$$\nabla \cdot \mathbf{v} = 0, \tag{2}$$

for any isothermal, viscous, incompressible, Newtonian fluid, where $\mathbf{v}$ represents velocity, p pressure, ρ fluid density, and μ dynamic viscosity.

As shown in previous work (Marlevi et al., 2019), virtual work-energy can be evaluated by introducing an auxiliary, arbitrary virtual velocity field $\mathbf{w}$, multiplying it with Eq. (1), and integrating the resulting expression over the entire fluid domain Ω, with boundaries Γ and normal $\mathbf{n}$. Doing so, the remaining energy-balance can, after integration-by-parts, be expressed as

$$\frac{\partial K_e}{\partial t} + A_e - S_e + V_e + H(p) = 0, \tag{3}$$

with

$$\frac{\partial K_e}{\partial t} = \rho \int_\Omega \frac{\partial \mathbf{v}}{\partial t} \cdot \mathbf{w} \, d\Omega \tag{4}$$

$$A_e = \rho \int_\Omega (\mathbf{v} \cdot \nabla \mathbf{v}) \cdot \mathbf{w} \, d\Omega \tag{5}$$

$$S_e = \mu \int_\Gamma (\nabla \mathbf{v} \cdot \mathbf{n}) \cdot \mathbf{w} \, d\Gamma \tag{6}$$

$$V_e = \mu \int_\Omega \nabla \mathbf{v} : \nabla \mathbf{w} \, d\Omega \tag{7}$$

$$H(p) = \int_\Gamma p\mathbf{w} \cdot \mathbf{n} \, d\Gamma - \int_\Omega p \nabla \cdot \mathbf{w} \, d\Omega. \tag{8}$$

Eqs. (4)–(8) represent different *virtual* energy components in the assessed system: K_e the *virtual* kinetic energy, A_e the *virtual* advective energy rate, S_e the *virtual* power transfer due to shear, V_e the rate of *virtual* viscous energy dissipation, and $H(p)$ the *virtual* input hydraulic power.

The pressure difference Δp between two arbitrarily selected planes Γ_i and Γ_o can then be computed by assigning certain properties to the virtual field **w**. By selecting **w** such that

1. **w** is a strictly solenoidal field, satisfying $\nabla \cdot \mathbf{w} = 0$
2. $\mathbf{w} = 0$ at Γ_w (where Γ_w is the assigned domain boundary walls, given by splitting the complete domain boundary Γ into $\Gamma = \Gamma_i \cup \Gamma_o \cup \Gamma_w$)

we can re-express Eq. (8) into

$$H(p) = (p_i - p_o) \int_{\Gamma_i} \mathbf{w} \cdot \mathbf{n} \, d\Gamma = \Delta p Q, \tag{9}$$

where Q is the total inflow of **w** through Γ_i, and where the expression is derived by noting that $Q_i = Q_o$ following Eq. (12) (imposing mass conservation of **w**). Noteworthy is that Eq. (9) assumes pressure to be constant over Γ_i and Γ_o, respectively; a reasonable assumption when probing short-axis sections in the heart. However, in the instance that pressure varies over Γ_i or Γ_o, Eq. (8) is not invalidated but rather represents the extraction of the *weighted mean* pressure over each plane, respectively; again being possibly valuable in clinical usage.

Continuing, by assigning **w** such that

3. **w** is aligned to the surface normal direction at Γ_i and Γ_o

along with the fact that $\mu \nabla \mathbf{v} \cdot \mathbf{n}$ is generally small at Γ_i and Γ_o, we can assign Eq. (6) to be $S_e \approx 0$. As such, Eq. (3) can be re-arranged into the final formulation of νWERP, reading

$$\Delta p = -\frac{1}{Q} \left(\frac{\partial K_e}{\partial t} + A_e + V_e \right). \tag{10}$$

Note that all entities at the right-hand side of in Eq. (10) can be directly derived from the acquired flow field **v**. The only thing that has to be externally added is the virtual field **w**, being generated in such a way that it abides to all the previously enumerated properties. In theory, an infinite number of **w** exists that fulfills these properties, however, for simplicity, we choose to assign **w** as the solution to a Stokes problem defined by

$$\nabla^2 \mathbf{w} + \nabla \lambda = 0 \tag{11}$$

$$\nabla \cdot \mathbf{w} = 0 \tag{12}$$

$$\mathbf{w} = \begin{cases} -\mathbf{n}, & \Gamma_i \\ 0, & \Gamma_w \end{cases} \tag{13}$$

where λ is the virtual pressure field corresponding to **w**. Here, a plug inflow is defined at Γ_i, assigned in the normal direction **n**. At Γ_o a Neumann condition is defined ($\mu \nabla \mathbf{w} \cdot \mathbf{n} - \lambda \mathbf{n} = 0$), ensuring a well-posed setup.

2.2. Extension of νWERP to dynamic domains using arbitrary lagrangian-Eulerian formulation

In Section 2.1, the Navier-Stokes equations were provided in a purely Eulerian form where each entity is represented as a function of space and time on a well-defined static domain Ω. In comparison, when dealing with fluid flow over a *dynamically moving domain* - such as in the case of intracardiac blood flow - we can instead use the Arbitrary Lagrangian-Eulerian (ALE) form of Navier-Stokes equations, expressed over the dynamic domain $\Omega = \Omega(t)$. The two are theoretically identical, however refer to different reference frames (the Eulerian using a fixed grid over which fluid passes, the ALE using a projected grid that incorporates the movement of the fluid domain). As such, this ALE-form, or non-conservative form of the Navier-Stokes equations can be expressed as

$$\rho \ \partial_t \mathbf{v} + \rho (\mathbf{v} - \mathbf{u}) \cdot \nabla \mathbf{v} - \mu \nabla^2 \mathbf{v} + \nabla p = 0, \tag{14}$$

$$\nabla \cdot \mathbf{v} = 0, \tag{15}$$

where **u** describes the velocity of the dynamic domain $\Omega(t)$. Herein, it is imperative to note that the temporal derivative ∂_t in Eq. (14) refers to a fixed point in the created ALE domain, and is *not* equivalent to the temporal derivative in Eq. (1). Instead, as shown by others (Hirt et al., 1974), the two are related as

$$\partial_t \mathbf{v} = \frac{\partial \mathbf{v}}{\partial t} + \mathbf{u} \cdot \nabla \mathbf{v}, \tag{16}$$

again, having to take the movement **u** of the reference domain into consideration (extracted by e.g. harmonic extension). The ALE frame that ∂_t is referring to can be viewed as a fixed reference domain Λ, itself connected to the dynamic domain $\Omega(t)$ through an arbitrary mapping $M : \Omega(t) \to \Lambda$. In practical use, Eqs. (14)–(15) are therefore solved by identifying the mapping M, along with the domain movement.

For the sake of νWERP, the transition into an ALE-formulation does not represent any theoretical hindrance, and the derivation of virtual work-energy in Section 2.1 still holds. The difference between Eq. (1) and Eq. (14) will however modify the expression of kinetic (K_e) and advective (A_e) virtual energy, to instead read

$$\partial_t K_e = \rho \int_\Omega \partial_t \mathbf{v} \cdot \mathbf{w} \, d\Omega \tag{17}$$

$$A_e = \rho \int_\Omega ((\mathbf{v} - \mathbf{u}) \cdot \nabla \mathbf{v}) \cdot \mathbf{w} \, d\Omega. \tag{18}$$

Importantly, the final expression of νWERP given by Eq. (10) still holds. Similarly, the properties assigned to **w** (1.-3. in Section 2.1) will not be violated by the transition into an ALE form, and neither will the definition of **w** as a Stokes flow be influenced. However, since the domain of interest $\Omega(t)$ is now dynamically changing over time, the domain boundaries Γ_i, Γ_o, and Γ_w used to construct **w** will also have to be continuously updated, and Eq. (11)–(13) will also have to be re-evaluated at each discrete time step.

The ALE-form of the Navier-Stokes equations has been extensively used to treat dynamically moving flow domains in a plethora of disciplines, however, the formulation has proven particularly useful in the computational assessment of intracardiac flow (Khalafvand et al., 2011). For νWERP, utilizing a complete ALE-formulation would sufficiently cover the issue of dynamic domains, and the expression would be invariant to the magnitude of the imposed domain movement. Similarly, mapping the acquired velocity field onto an ALE framework would mean that the entire velocity field could be maintained within the νWERP evaluation, thereby maximizing effective signal-to-noise ratio. However, utilizing an ALE-formulation would also come with some practical drawbacks. In particular, when dealing with discretized flow data the introduction of the arbitrary mapping M complicates computation, where non-trivial interpolation has to be introduced to map how $\mathbf{v}$ and the spatial gradients $\nabla\mathbf{v}$ change along the spatiotemporal trajectory of M. Similarly, an ALE-based νWERP would be computationally more demanding, as the inclusion of $\mathbf{u}$ and ∂_t makes the derivation of the virtual energy components more involved, and since the method requires inherent recalculation of $\mathbf{w}$ for each defined time step.

2.3. Extension of νWERP to dynamic domains using sub-domains

In the previous sections, it is imperative to understand that these descriptions are typically utilized to described a *complete* fluid domain, where flow is restricted to a boundary-conforming spatiotemporal domain Ω. In such a setting, the Eulerian formulation can be utilized when assessing the *complete* flow through an assumed, non-compliant vascular section (see e.g. (Shahcheraghi et al., 2002)), and the ALE formulation can be utilized when describing the *complete* intracardiac motion of blood (see e.g. (Khalafvand et al., 2011)).

However, if we remain in the dynamic domain of $\Omega(t)$, an Eulerian description could still be utilized as long as we limit ourselves to a *sub-domain* $\Omega_s \subset \Omega(t)$ that maintains static over the assessed time frame. That is, as long as we are satisfied with only assessing flow over Ω_s, we can maintain an Eulerian description of the flow within that particular sub-domain. In theory, Ω_s can take any form that satisfies $\Omega_s \subset \Omega(t)$. However, when working with discretized image data, we can in practice define two alternative approaches.

As a first approach, we can assign Ω_s to be a *dynamic domain intersect* (DDI), representing the intersect between domains of consecutive image frames, such that

$$\Omega_s = \Omega(t_i) \cap \Omega(t_{i+1}), \tag{19}$$

where $\Omega(t_i)$ and $\Omega(t_{i+1})$ represent the complete, dynamic domain at time t_i and t_{i+1}, respectively. Thus, Ω_s represents a sub-domain at any given time $t \in [t_i, t_{i+1}]$ (as an illustration, see Fig. 1).

As a second approach, we can assign Ω_s to be the *static domain intersect* (SDI) of *all* image frame domains, such that

$$\Omega_s = \Omega(t_0) \cap \Omega(t_1) \cap \Omega(t_2) \cap \ldots \cap \Omega(t_n), \tag{20}$$

where t_0 and t_n represent the first and last time frame of the flow acquisition, respectively. As such, Ω_s in the SDI approach holds for any given time t (see again Fig. 1 for an illustration).

It is important to note that both DDI and SDI requires Ω_s to be a true *sub-set* of $\Omega(t)$. If we instead would assign Ω_s as the *super-set* of the true dynamic domain (e.g. $\Omega_s = \Omega(t_i) \ \cup \ \Omega(t_{i+1})$), it is no longer certain that Ω_s stays within the assessed flow domain $\Omega(t)$. As such, the Eulerian approach would no longer hold true, and for νWERP in particular, evaluations over domain boundaries Γ will no longer be valid.

However, as long as $\Omega_s \subset \Omega$, any flow within Ω_s can be accurately described using an Eulerian approach. Consequently, if limiting our assessment of relative pressures to within Ω_s, νWERP as derived and described in Section 2.1 holds true. Similarly, the transition into computations on sub-domains does not obstruct any of the required properties assigned to $\mathbf{w}$. Instead, the sub-domain approach enables all virtual energy components to remain in the original Eulerian formulation (Eqs. (4)–(8)), and the derivation of relative pressure is thus - yet again - governed by Eq. (10). As such, the sub-domain approach shows an inherent benefit over the complete ALE-formulation, avoiding the need for an introduced domain mapping M and any associated interpolation of $\mathbf{v}$. Similarly, utilizing sub-domains avoids inclusion of the domain movement $\mathbf{u}$, along with its associated computational complexity.

In addition to the benefits shown over the ALE-formulation of νWERP, the DDI and SDI approach come with their own particular advantages. For DDI - even though the sub-domain approach will inherently decrease the number of data points included in the νWERP computation - the approach in Eq. (19) will ensure that Ω_s is as inclusive as possible. On the other hand, with Eq. (19) describing a continuously updated sub-domain, $\mathbf{w}$ will have to be subsequently recalculated as νWERP is advanced over time.

By contrast, the SDI approach will be limited by the size of Ω_s, where Eq. (20) restricts computation to an intersect of all possible time frames. In the case of large deformations or significant translations, this will drastically reduce the number of data points included in the νWERP computation. However, this might not be an inherent hindrance to any intracardiac implementation, where excessive domain motion is typically rare over a physiological cardiac cycle (Arts et al., 1992). Instead, a benefit of the SDI approach is that Ω_s is inherently static, meaning that a single $\mathbf{w}$ can be uti-

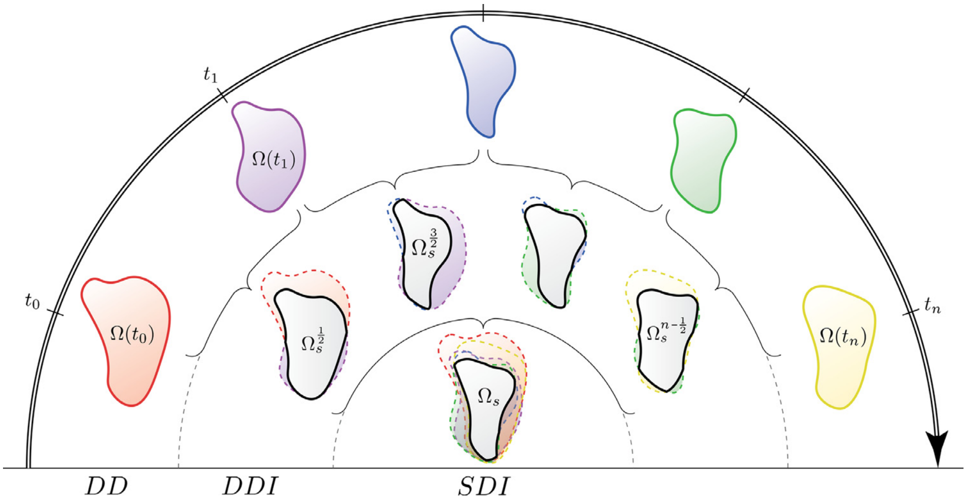

Fig. 1. Illustration of sub-domain approach to handle dynamic domains. With a temporal axis represented by the outer-most circular arc, the dynamic domain (Ω, section DD) changes extent over time. Using a dynamic domain intersect approach (section DDI), a series of sub-domains Ω_s are created from the intersect of consecutive frames t_i and t_{i+1}, such that each $\Omega_s^{i+\frac{1}{2}}$ is valid over $t \in [t_i, t_{i+1}]$. Using a static domain intersect approach (section SDI), a single sub-domain Ω_s is created as the intersect over all time frames t_0 to t_n. As such, Ω_s holds for $t \in [t_0, t_n]$.

lized over all time steps. As such, Eqs. (11)–(13) only has to be solved once for the entire νWERP computation, reducing the computational effort in deriving relative pressure.

2.4. Computation of νWERP on dynamic domains using full field data

Details of the numerical implementation of νWERP on static fields is outlined elsewhere (Marlevi et al., 2019), however, below follows a brief summary of this procedure for the extension into dynamic domains.

2.4.1. Data processing and dynamic domain segmentation

As formulated, νWERP acts directly on acquired full field data, and does not require any additional input data collection. However, to appropriately assess the dynamic fluid domain, a set of image-processing steps are required.

(i) *Domain segmentation* - The dynamic fluid domain has to be segmented in the provided full field data. For the intracardiac space, a wide variety of segmentation approaches exists ranging from complete manual assessment to automated deterministic and learned methods (Petitjean and Dacher, 2011; Zotti et al., 2018; Bustamante et al., 2018). νWERP is however not tied to any specific approach, but can instead be utilized with any segmentation scheme of choice. For the sake of dynamic domains, segmentations are provided as a 4D entity, describing the dynamic movement of a 3D binary segmentation over time. From these, sub-domain segmentations can then be generated in accordance with either the DDI or SDI approach.

(ii) *Definition of inlet and outlet plane* - To determine over which region pressure drops are to be calculated, inlet and outlet planes have to be indicated in the segmented flow fields. Most practically, these can be manually selected within the 4D segmentations, and then propagated onto each respective sub-domain segmentations.

(iii) *Domain labelling* - To assign boundary conditions in the computation of $\mathbf{w}$, all voxels within the segmented domain have to be classified as either interior (being completely within the fluid sub-domain), exterior (being completely outside the fluid sub-domain), inlet or outlet (being part of the defined inlet or outlet planes), or wall (separating interior and exterior), respectively.

2.4.2. Computation of virtual field

Using the sub-domain approach, the computation of $\mathbf{w}$ does not differ from what has been previously reported. The Stokes problem of Eqs. (11)–(13) is solved using a staggered grid Finite Difference Method (FDM), with boundary conditions projected onto the discretized full field data utilizing the domain labelling in Section 2.4.1. To reduce numerical errors in the FDM solution, data subsampling was employed, such that $\mathbf{w}$ was solved on an upsampled version of the provided discretized domain. To exemplify, an upsampling factor of 2 would mean that a single image voxel is split by a factor of 2 in all spatial dimensions, effectively solving $\mathbf{w}$ on a grid with 2^3 times more voxels. Note that this upsampling does not affect the input data $\mathbf{v}$. Further details on this process can be found in the original νWERP publication (Marlevi et al., 2019).

2.4.3. Numerical implementation

To utilize νWERP on acquired flow field data, the expressions in Section 2.1 have to be re-reformulated in a discretized, spatiotemporal format. This includes defining DDI or SDI sub-domains, extracting temporal and spatial derivatives, and evaluating virtual energy components, all within the provided spatiotemporal domain. Specifics of such are given in Appendix A, however, important to note is that νWERP is solely based on provided flow data and associated segmentation, meaning that no additional input information is required in order to compute relative pressure.

2.5. Verification and spatiotemporal analysis using a simplified dynamic domain benchmark problem

For the extension of νWERP onto dynamic domains, a first set of validation tests were performed. For this, an analytical *in-silico* benchmark problem was designed, where the dynamic domain movement could be described by a universally applicable, analytical expression.

In short, the benchmark problem was designed as a spherical fluid filled domain, where flow was allowed to enter and exit through a capped top surface. By imposing a prescribed wall motion onto the spherical boundaries - deforming the capped sphere into a biconcave disc - flow entered and exited the domain over time, creating a varying velocity and pressure field within the dynamically shifting domain.

To theoretically prescribe the wall motion, a 3D sphere with radius R_0 was created, defined at time t_0 and given in Cartesian coordinates (x, y, z). The domain was cut at $z > 0.9R_0$, creating a capped planar surface section at $z = 0.9R_0$. The imposed wall motion was for simplicity restricted to the y direction, defined by

$$y(x, y, z, t) = y(1 - f(t)) + S(x, y, z)f(t)y_R, \tag{21}$$

where $y_R = y/\sqrt{R_0^2 - r^2}$ is the distance from the *xz*-plane normalized by the local thickness (used to ensure that the spatial transformation is injective, and assigning $r = \sqrt{x^2 + z^2}$ as the *xz*-plane radial coordinate), $f(t) = \sin^2(\pi t/T)$ acts as a weighting between the undeformed and maximally deformed states, and T is the length of one temporal cycle. Note that as $f(t)$ has an argument of $\pi t/T$, maximum deformation occurs at $t = 0.5T$, with the original undeformed state recovered at $t = T$.

In Eq. (21), the function S represents the shape of the domain's boundary at peak deformation, given by

$$S(x, y, z) = \frac{r^2\sqrt{R_0^2 - r^2} + h(R_0 + r)(R_0 - r)}{R_0^2}. \tag{22}$$

Here, $h \in [0, R_0]$ is a magnitude coefficient, used to scale the degree of deformation. To obtain visibly sufficient deformation, the magnitude coefficient was set as $h = 0.2R_0$, $R_0 = 25$ mm, and $T = 0.5$ s. An overview of the created domain, velocity, and pressure field, is given in Fig. 2.

Using the above, flow was computed inside the dynamic domain by Computational Fluid Dynamics (CFD) simulations using a cG(1)cG(1) method (Hessenthaler et al., 2017) for solving the incompressible Navier-Stokes equations in an ALE coordinate frame (technical details are provided in Appendix B). Simulations were run for ten cycles to ensure steady state, with data extracted from the final 10th cycle. Synthetic image data - consisting of a voxelized velocity and pressure field, respectively - was created by projecting the CFD output onto a uniform image grid. To study the effect of spatiotemporal sampling, data was generated at 1, 2, 3, and 4 mm^3, with temporal sampling of 10, 20, 25, and 50 ms, respectively.

For each set of spatiotemporal sampling, pressure drops were computed between the capped surface at $z = 0.9R_0$ and a corresponding planar surface within the fluid domain at approximately $z = -0.9R_0$. Using νWERP, both the DDI and SDI sub-domain approach was used, evaluating potential differences between the two. To ensure that the spatial convergence analysis was not influence by the numerical accuracy of $\mathbf{w}$, individual levels of domain subsampling was applied at the each level of spatial sampling (description on the domain subsampling is given in Section 2.4.2).

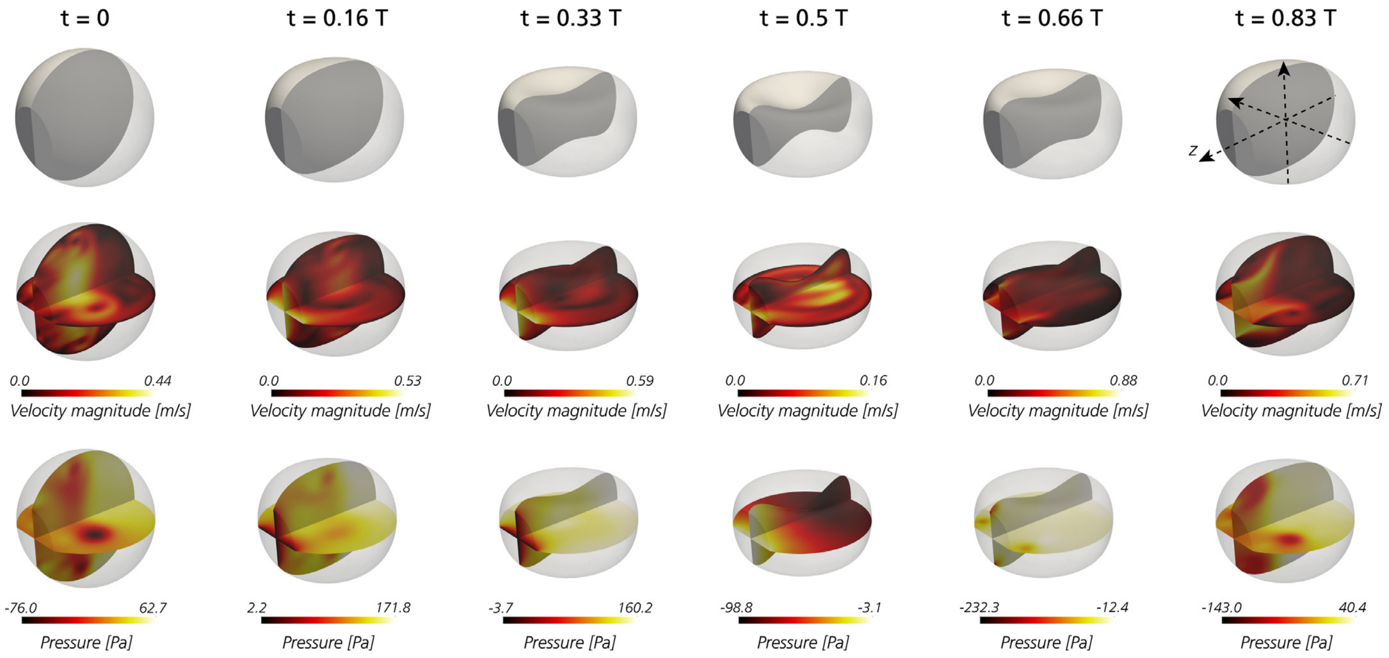
t = 0
t = 0.16 T
t = 0.33 T
t = 0.5 T
t = 0.66 T
t = 0.83 T
z
0.0
0.44
Velocity magnitude [m/s]
0.0
0.53
Velocity magnitude [m/s]
0.0
0.59
Velocity magnitude [m/s]
0.0
0.16
Velocity magnitude [m/s]
0.0
0.88
Velocity magnitude [m/s]
0.0
0.71
Velocity magnitude [m/s]
-76.0
62.7
Pressure [Pa]
2.2
171.8
Pressure [Pa]
-3.7
160.2
Pressure [Pa]
-98.8
-3.1
Pressure [Pa]
-232.3
-12.4
Pressure [Pa]
-143.0
40.4
Pressure [Pa]

Fig. 2. Overview of the dynamic domain benchmark problem, created to evaluate νWERP performance over dynamic domains. The domain is initiated as a capped spherical domain ($t = 0$), which is then deformed into a biconcave disc (maximum deformation at $t = 0.5T$), before returning to its original state ($t = T$). With the deformation, internal fluid is allowed to enter and exit through the capped side surface, creating a varying $\mathbf{v}$ and p-fields inside the domain. Top row: Surface rendering of dynamic domain. Middle row: Perpendicular cuts through the domain, showing velocity magnitude over the temporal cycle. Bottom row: Perpendicular cuts through the domain, showing the pressure field over the temporal cycle. Coordinate axes are given at the top right.

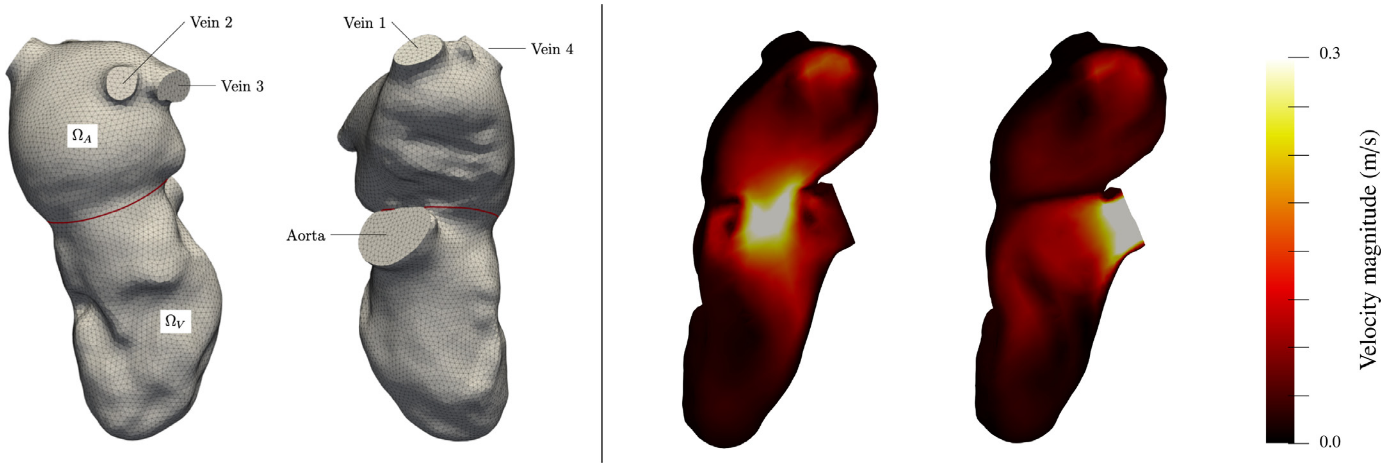
Vein 2
Vein 3
Vein 1
Vein 4
Ω_A
Ω_V
Aorta
0.3
0.0
Velocity magnitude (m/s)

Fig. 3. Left: Patient-specific left heart model, including the left atrium (Ω_A) and left ventricle (Ω_V), showing initial mesh and the different inflow and outflow boundaries at pulmonary veins and the aorta. The red line indicates the coupling surface between atrium and ventricle. Figure from Hessenthaler (2020). Right: Velocity magnitude at $t = 0.16$ s and $t = 0.64$ s at a section cutting the MV surface and AV outflow boundary. (For interpretation of the references to colour in this figure legend, the reader is referred to the web version of this article.)

2.6. Verification and noise analysis using a patient-specific left heart model

To further study the extension of νWERP onto dynamic domains, and to specifically evaluate performance in a realistic flow scenario, a patient-specific CFD model of the left heart was utilized.

2.6.1. Numerical setup and initial assessment

For this study, the left atrium (LA) and left ventricle (LV) domains, see Fig. 3, were extracted from computed tomography (CT) data of a cardiac resynchronization therapy (CRT) patient, suffering from abnormal wall motion and reduced ejection fraction (EF = 20.8%). With original image data provided at a resolution of 10 frames/cardiac cycle, motion of the outer walls was generated at 1 ms increments by means of local B-spline interpolation. Cardiac cycle time was 0.8 s with systole lasting for the first 0.43 s, and diastole lasting for the remaining 0.37 s. The fluid density and viscosity were selected as $\rho = 1025$ g/cm^3 and $\mu = 4$ mPa $\cdot$ s.

Similar to Section 2.5, flow in the LA and LV was modeled using the incompressible Navier-Stokes equations in ALE form with a cG(1)cG(1) stabilization approach. Note that LA and LV were treated as two definite sub-domains, where coupling was enforced using a Lagrange multiplier. Valve leaflets were not incorporated into the model, and instead the switch in valve opening between systole and diastole was assumed instantaneous for both mitral and aortic valve, respectively (technical details on the CFD setup are provided in Appendix C). To ensure periodic steady state, simulations were run for seven cardiac cycles, with data extracted from the final one. Synthetic image data was created for LA and LV separately, projecting the CFD velocity and pressure output onto a uniform image grid in a similar fashion to Section 2.5. To mimic realistic imaging settings, data was sampled at 2 mm^3, with temporal sampling of 29.6 ms (extracting 27 frames over the simulated cardiac cycle).

As an initial assessment, pressure drops were computed for four different sections, using both νWERP DDI and SDI approach:

1. From the mitral valve (MV) to a distal apical plane of the LV
2. From a distal apical plane of the LV to the aortic valve (AV) outlet
3. From the left inferior pulmonary vein inlet, to the MV
4. From the left superior pulmonary vein inlet, to the MV

Here 1. and 2. were chosen to represent LV, and 3. and 4. LA behavior, respectively.

2.6.2. Noise sensitivity analysis

To evaluate the effect of random image fluctuations on νWERP output, synthetic image noise was added to computed image data of the left heart. By assigning a synthetic velocity encoding at v_{enc} = 1.5 m/s, and utilizing the fact that v_{enc} relates to velocity standard deviation σ and signal-to-noise-ratio (SNR) as

$$\sigma = \frac{\sqrt{2}v_{enc}}{\pi \cdot SNR}, \tag{23}$$

σ could be derived for three different noise-scenarios: low-noise (SNR = 25), mid-noise (SNR = 15) and high-noise (SNR = 5). At each SNR-level, noise was distributed over all voxels and all frames of the synthetic image data following a truncated Gaussian distribution, with standard deviation given by σ, and with truncation applied for $[-2\sigma, 2\sigma]$ to avoid spurious noise effects. At each noise-level, the synthetic image data was amended with 50 different noise fields, generating pressure drop assessments for each sample. As such, output could be generated as mean ± standard deviation. For simplicity, the evaluation of noise was only performed in the LV, probing pressure drops from MV to a distal apical planen using both the νWERP DDI and SDI approach.

2.6.3. Effect of sub-domain extent

In all aforementioned tests, the SDI approach of νWERP utilized the *largest possible sub-domain* Ω_s, created as the intersect of $\Omega(t)$ over all time frames, as per Eq. (20). However, we posed the question of how the extent of Ω_s would affect the output of νWERP and the SDI approach.

To evaluate this, the setup in Section 2.6.2 was again utilized, probing the pressure drop from MV to an apical plane in the patient-specific left heart model. Using the largest possible subdomain Ω_s (again created from the intersect over all frames as per Eq. (20)), a set of *additional* domains were now created by either

1. *Eroding* the domain around the MV-apical axis
2. *Dilating* the domain around the MV-apical axis

In practice, that meant that in 1., the outer-most layer of Ω_s was effectively removed, creating a smaller Ω_s for the SDI approach. Conversely, in 2. an additional outer layer was added to Ω_s, creating a larger Ω_s for the SDI approach (note that in this instance, $\Omega_s \cap \Omega(t)$ will no longer hold). A visualization of how this changed the assessed SDI domain is shown for three-layer erosion/dilation in Fig. 4.

In both instances, modifications were made by dilating or eroding up to four layers around the MV-apical axis. In each instance, the MV-apical pressure drop was assessed, along with a noise sensitivity analysis as in Section 2.6.2. Note that the position of the inlet and outlet planes (between which relative pressure was computed) did not change despite any eroded or dilated domain. Instead, the planes were expanded or reduced in cross-section to fit the extent of each sub-domain set, respectively. Furthermore, in order to ensure complete convergence in the creation of $\mathbf{w}$ - independent of domain extent - additional levels of domain subsampling (as described in Section 2.4.2) was applied on the eroded sub-domains (using a subsampling factor of 2 on the 1–2 level erosion; using a subsampling factor of 3 on the 3–4 level erosion).

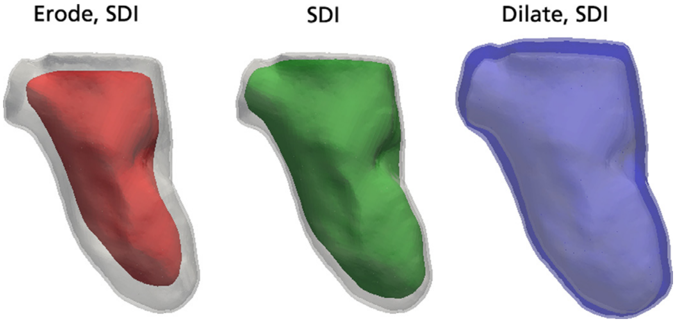

Fig. 4. The νWERP SDI approach was evaluated as a function of sub-domain size. The dynamic domain Ω at onset of systole is shown in gray, the largest possible sub-domain Ω_s as per Eq. (20) is shown in green (mid panel). Removal of a set of outermost voxels (erosion) creates a more conservative, smaller domain, shown in red (left panel). Dilation of outermost voxels creates a more inclusive, larger domain, shown in blue (right panel). Note that the larger blue domain is no longer a sub-domain of Ω. (For interpretation of the references to colour in this figure legend, the reader is referred to the web version of this article.)

2.7. Application to intraventricular flows in vivo using 4D flow MRI

To test νWERP as a tool for clinical intracardiac assessment, the method was applied on *in-vivo* data from 4D Flow MRI sessions. Data was retrospectively collected from 5 healthy subjects (EF = $62.7 \pm 3.4\%$, EA-ratio = 1.36 ± 0.25) and 1 patient exhibiting signs of diastolic dysfunction through impaired relaxation (EF = 60.2%, EA-ratio = 0.65). The set of healthy subject were used to test output consistency, whereas the patient case was used as a feasibility test, indicating possible differences in the assessed intracardiac pressure drops by νWERP.

For all subjects, images were acquired using a 3T Philips Ingenia system (Philips Healthcare, Best, the Netherlands). The field-of-view was adjusted to cover the entire thoracic cavity, centered on the heart, with acquired spatiotemporal resolution of 2.7x2.7x2.8 mm^3 and 52.8 ms, respectively. Acquired data was corrected for concomitant gradients fields, phase wraps, as well as background phase errors. Further details on data collection can be found in previous work (Bustamante et al., 2015).

A validated multi-atlas segmentation technique was used to segment intracardiac chambers, as well as great thoracic vessels in all image sets (Bustamante et al., 2015; 2018). Focusing on the LV, pressure drops were computed:

1. From the MV to a distal apical plane
2. From a distal apical plane to the AV

To facilitate this, the interface between LA and LV segmentation was used to define the MV plane. Similarly, the interface between LV and aortic segmentation was used to define the AV opening. The apical plane was manually positioned at a distal part of the LV, qualitatively parallel to the atrioventricular plane, and ensuring that it remained inside the LV throughout the cardiac cycle. Based on the *in-silico* results, the sub-domain SDI approach was used for all νWERP computations. A resampling factor of $n = 2$ was used for the subsampling of $\mathbf{w}$.

2.8. Alternative methods for estimation of intracardiac relative pressure

To compare νWERP output against alternative approaches, relative pressure was in all instances derived using two other, previously proposed methods for intracardiac analysis.

First, relative pressure was assessed using a reduced Bernoulli (RB) formulation. Under this formulation, the relative pressure Δp between two points $\mathbf{q}_i$ and $\mathbf{q}_o$ in Γ_i and Γ_o, respectively, is estimated as

$$\Delta p(t) = \frac{1}{2}\rho\left(v_o^2(t) - v_i^2(t)\right), \tag{24}$$

where $v_k(t) = \mathbf{v}(\mathbf{q}_k, t) \cdot \mathbf{n}$ (with $k = o, i$ and $\mathbf{n}$ denoting the unit vector from $\mathbf{q}_i$ to $\mathbf{q}_o$). While the reduced Bernoulli formulation introduces a number of simplifications regarding the flow, it also has the smallest requirements on measurement data, resulting in its popular application.

In addition to RB estimates, relative pressure was also assessed using the unsteady Bernoulli (UB) equation, representing an extension of Eq. (24) including inertial terms appearing in the momentum balance (Firstenberg et al., 2001). In this case, the pressure drop between $\mathbf{q}_i$ and $\mathbf{q}_o$ is computed by considering the integration of the inertial term along an integration line $\mathbf{p}(s)$ (where s is a parametric coordinate such that $\mathbf{p}(0) = \mathbf{q}_i$ and $\mathbf{p}(1) = \mathbf{q}_0$). In UB, the pressure is approximated as

$$\Delta p = \frac{1}{2}\rho\left(v_o^2(t) - v_i^2(t)\right) + \rho \int_0^1 \frac{\partial \mathbf{v}}{\partial t} \cdot \frac{\partial \mathbf{p}}{\partial s}\, ds. \tag{25}$$

As before, v_o and v_i are the velocities projected in the direction of $\mathbf{n}$ at $\mathbf{q}_o$ and $\mathbf{q}_i$, respectively. For simplicity, $\mathbf{q}_i$ and $\mathbf{q}_o$ were assigned as the mid-points on Γ_i and Γ_o, respectively, with s being a straight integration line along $\mathbf{n}$. If by using this definition, $\mathbf{p}(s)$ went outside the domain Ω, $\mathbf{p}(s)$ was split into two sections: one from $\mathbf{q}_i$ to the mid-point of the domain $\Omega(t)$, and one from the mid-point of $\Omega(t)$ to $\mathbf{q}_o$.

2.9. Statistical analysis

For the validation in both the dynamic domain benchmark problem and patient-specific left heart model *in-silico* setup, an estimate of mean similarity was calculated by the normalized Fréchet distance, d_f, given as

$$d_f = \frac{\inf_{\Delta p, \Delta p_e} \max_{t\in[t_0,t_n]} ||\Delta p(t) - \Delta p_e(t)||}{\inf_{\Delta p} \max_{t\in[t_0,t_n]} ||\Delta p(t)||}. \tag{26}$$

Here, Δp is the true relative relative pressure, and Δp_e is the corresponding estimated output, both given as a function of time t. As such, d_f measures the *average distance* between Δp and Δp_e over the entire temporal cycle T, normalized by the distance between Δp and a reference null-estimate ($\Delta p_e = 0$). To enrich the evaluated data, Δp_e and Δp were temporally upsampled to the equivalent of 1 ms, achieved by piece-wise linear interpolation. Similarly, for the spatiotemporal convergence analysis in the dynamic domain benchmark problem, true data Δp was always represented by the CFD data obtained at the highest-most spatiotemporal sampling (given at 1 mm^3 and 10 ms, respectively). Furthermore, to ensure fair comparison between methods, true Δp for νWERP was given as the mean pressure drop between Γ_i and Γ_o, whereas for RB and UB, true Δp was given as the pressure drop between $\mathbf{q_i}$ and $\mathbf{q_o}$.

For the patient-specific left heart model, errors in maximum and minimum pressure drop were also assessed by

$$\varepsilon(\Delta P_{max/min}) = \left(\frac{|\Delta p_e(t_m) - \Delta p(t_m)|}{|\Delta p(t_m)|}\right), \tag{27}$$

where t_m is the time at either maximum or minimum pressure drop for the true estimate Δp, respectively. To provide a 1:1 comparison with the estimated pressure drops, the true estimate Δp was in this instance extracted from a voxelized pressure field, obtained by sampling the generated CFD solution at identical spatiotemporal sampling (2 mm^3, 29.6 ms).

Furthermore, for the patient-specific left heart model, the root mean square error was calculated as

$$\varepsilon_{rmse} = \frac{1}{N}\sqrt{\sum_{n=1}^{N} (\,|\Delta p_e - \Delta p_n|\,)^2}. \tag{28}$$

Lastly, data from the dynamic domain benchmark problem and the patient-specific left heart model was combined, and linear regression was assessed between predicted and true pressure drop. To represent realistic imaging settings, data was only combined for a spatial sampling of 2 mm^3 or higher. Additionally, Bland-Altman plots were generated on the same combined data to assess potential method bias.

Complete data analysis and implementation was performed in MATLAB R2016a (MathWorks, Natick, MA, USA).

3. Results

The following section provides results for the evaluation of νWERP on the dynamic domain benchmark problem (Section 3.1), on the patient-specific left heart simulation (Section 3.2), a cumulative assessment of the two (Section 3.3), and on the *in-vivo* 4D Flow MRI data (Section 3.4), respectively.

3.1. Dynamic domain benchmark problem

Estimations of relative pressure through the dynamic domain benchmark problem are given for νWERP using both the DDI and SDI approach, as well as for the alternative UB and RB approaches in Table 1, with output given as d_f at different spatiotemporal sampling. As an example of the relative pressure development over time, Fig. 5 presents output at 2mm^3 spatial sampling, and 20 ms temporal sampling (picked to represent routinely acquired 4D Flow MRI sampling). Note that for νWERP, true ΔP is represented by the mean ΔP between Γ_i and Γ_o, whereas in the Bernoulli instances, true ΔP is given by the estimated drop between the mid-points on Γ_i and Γ_o, respectively.

Overall, νWERP shows consistently high accuracy, with an average d_f of 16.0% over all evaluated instances (largest $d_f = 37.8\%$ at 3 mm^3 and 50 ms sampling, smallest $d_f = 6.3\%$ at 1 mm^3 and 10 ms sampling), corresponding to an absolute error in relative pressure smaller than 0.01 mmHg. For typical ranges of *in-vivo* full-field imaging (2 mm^3, 25 ms), d_f are below 14.7%.

In general, νWERP output improves with refined spatiotemporal sampling. Further, only minor differences can be inferred between DDI and SDI approach. For the assessment of the mean similarity error, SDI appear slightly more accurate over the entire spatiotemporal range (d_f ranging from 29.6% to 13.0% at 4mm^3 and 20.0% to 6.3% at 1mm^3 for DDI, compared to 22.1% to 8.4% at 4mm^3 and 15.9% to 10.9% at 1mm^3 for SDI, respectively). However, the difference in d_f is in average below 5.8%, indicating fairly similar output between the DDI and SDI approach.

With respect to spatiotemporal behavior, a minor favoring of temporal over spatial refinement seems apparent. Over the evaluated ranges, a twofold increase in spatial sampling (4 to 2, or 2 to 1 mm^3) rendered an average decrease in d_f by 45 and 20% for the DDI and SDI approach, respectively. In comparison, a twofold increase in temporal sampling (50 to 25 ms, or 20 to 10 ms) rendered an average decrease in d_f by 41 and 31% for the DDI and

Table 1

Numerical data for the estimation of relative pressure over the dynamic domain benchmark problem, given for νWERP with a DDI approach (first from left), νWERP with an SDI approach (second from left) approach, UB (third from left), or RB (fourth from left), respectively. Results are presented for the normalized Fréchet distance d_f, estimating the mean similarity between estimated and true relative pressure. Results are given as a function of spatial and temporal image sampling (1–4 mm^3 and 10–50 ms, respectively).

	νWERP - DDI				νWERP - SDI					UB				RB			
	$\mathbf{d_f}$				$\mathbf{d_f}$					$\mathbf{d_f}$				$\mathbf{d_f}$			
dx/dt	*50 ms*	*25 ms*	*20 ms*	*10 ms*	*50 ms*	*25 ms*	*20 ms*	*10 ms*	*dx/dt*	*50 ms*	*25 ms*	*20 ms*	*10 ms*	*50 ms*	*25 ms*	*20 ms*	*10 ms*
4 mm^3	29.6	15.4	13.1	13.0	22.1	10.8	8.2	8.4	***4 mm^3***	110.9	94.9	93.6	89.3	136.4	173.1	178.1	169.1
3 mm^3	37.8	28.2	28.8	28.4	14.5	14.4	14.6	15.6	***3 mm^3***	110.4	93.5	92.9	87.1	166.2	185.0	173.2	179.8
2 mm^3	23.2	14.6	14.6	14.7	15.7	11.7	11.2	10.5	***2 mm^3***	109.6	94.7	91.2	77.8	171.5	194.5	194.1	214.9
1 mm^3	20.0	8.5	6.5	6.3	15.9	13.2	12.0	10.9	***1 mm^3***	110.0	94.2	92.0	81.3	199.4	212.9	224.9	252.6

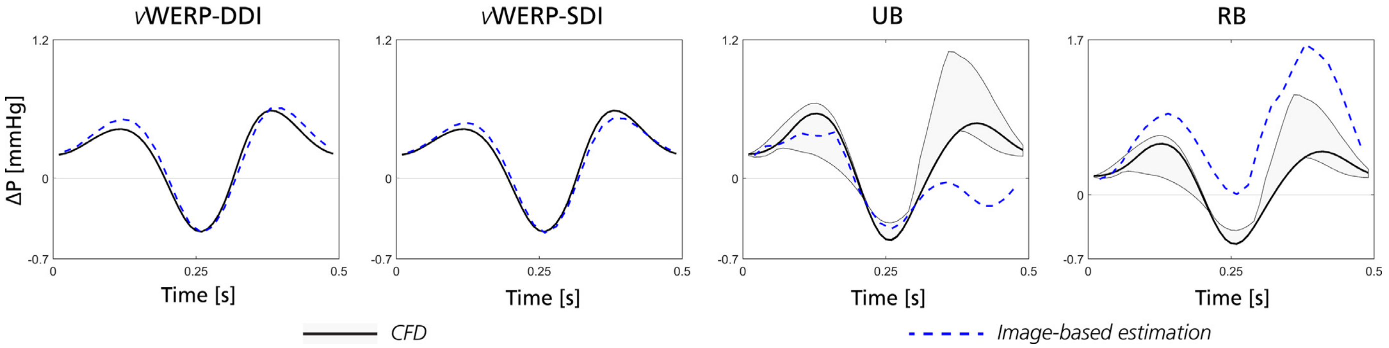

Fig. 5. Results from the dynamic domain benchmark problem, given for a spatiotemporal sampling of 2 mm^3 and 20 ms. Output given for, from left to right, νWERP using a DDI approach, νWERP using a SDI approach, UB, and RB, respectively. In each instance, comparative data from voxelized equivalents of the CFD pressure field is provided as reference: for νWERP comparisons are given against the mean pressure drop between Γ_i and Γ_o (black solid line), for UB and RB comparisons are given against a Γ_i mid-point Γ_o to mid-point pressure drop (black solid line) as well as an area showing the range of possible pressure differences between any two points at Γ_i and Γ_o (gray shaded area).

SDI approach, respectively. This improvement is particularly evident when increasing from 50 to 25 ms temporal sampling, where d_f decreases by up to 136%. Further refinement does not come with the same dramatic improvement, and d_f only decreases by 2% when increasing temporal sampling from 20 to 10 ms for both DDI ans SDI approach, respectively.

Over all evaluated spatiotemporal ranges, the alternative Bernoulli approaches show consistently higher normalized Fréchet distances. UB estimates are in average $d_f = 95.2\%$, with visually apparent deviations obvious in Fig. 5, especially towards the later half of the temporal cycle. RB shows more significant deterioration, with a systematic overestimation indicated in Fig. 5, and with d_f around or above 150% in a majority of all evaluated cases. The RB approach also does not indicate any visual spatiotemporal convergence where estimates are based purely on the resolved maximum velocities at inlet and outlet (as per Eq. (24)), highlighting the difficulty in utilizing the approach in a dynamically moving, complex flow domains.

3.2. Patient-specific left heart model

3.2.1. Assessment of left atrial and left ventricular relative pressure

Estimation of relative pressure in the patient-specific left heart model for a few selected sections are given in Fig. 6, with output shown for νWERP using a DDI approach, and for alternative UB and RB approaches, respectively. As visually apparent, νWERP provides accurate estimates in all evaluated sections, being able to handle flow behavior in both LA and LV throughout the cardiac cycle. Only minor deviations from the true relative pressure trace are observed, and in all sections peak maximum and minimum pressure drops are captured with an absolute error of below 0.1 mmHg, corresponding to $\varepsilon(\Delta P_{max/min}) = 11.0\%$ and 18.5% for LV and LA, respectively. UB shows similar ability to recover the transient changes of the true relative pressure, however, higher deviations seem apparent, and the accuracy in capturing peak pressure drops is slightly decreased ($\varepsilon(\Delta P_{max/min}) = 19.9\%$ and 59.9% for LV and LA, respectively). In comparison, RB is not able to replicate the transient behavior of the relative pressure trace, and even at peak events issues seem to prevail with respect to both under- and overestimation, as well as incorrect temporal positions (peak pressure drop absolute error of 0.4 mmHg, with $\varepsilon(\Delta P_{max/min}) = 61.2\%$ and 90.2% for LV and LA, respectively).

3.2.2. Noise sensitivity analysis

Complete data for the noise sensitivity study is given in Table 2, along with an output example given at SNR = 15 in Fig. 7.

In general, νWERP seems fairly invariant to added image noise, and exhibits consistent accuracy in all evaluated metrics, with only slightly decreased accuracy at the high-noise configuration (SNR = 5). The behavior is also not overly affected by the choice of DDI or SDI approach, where both show similar behavior in output. For DDI, d_f goes from 14.3% to 17.4 ± 4.0% when going from a noise-free (SNR = ∞) to a high-noise (SNR = 5) scenario; for SDI the same evaluation renders d_f values going from 13.5% to 19.8 ± 4.8%. Similar behavior is observed for the estimation of peak relative pressure, where no significant distortion is observed in $\varepsilon(\Delta P_{\max})$ or $\varepsilon(\Delta P_{\min})$. A slight opposite trend is seen for $\varepsilon(\Delta P_{\max})$ in the νWERP-SDI instance, however, the data should be contrasted to the absolute difference in estimate being within 0.02 mmHg. As such, the trend could be attributed to mere fluctuations at the discrete time representing $\Delta P_{\max}$, following the added Gaussian image noise. Regarding absolute errors, ε_{rmse} is also kept consistently below 0.01 mmHg, highlighting the noise-invariant behavior. Similarly, the added image noise does not generate a significant spread in output, and even at high noise (SNR = 5) standard deviations in d_f are kept below 5%.

Similar behavior can be observed for the assessments of peak pressure drop ($\varepsilon(\Delta P_{\max})$ and $\varepsilon(\Delta P_{\min})$). In this instance, the

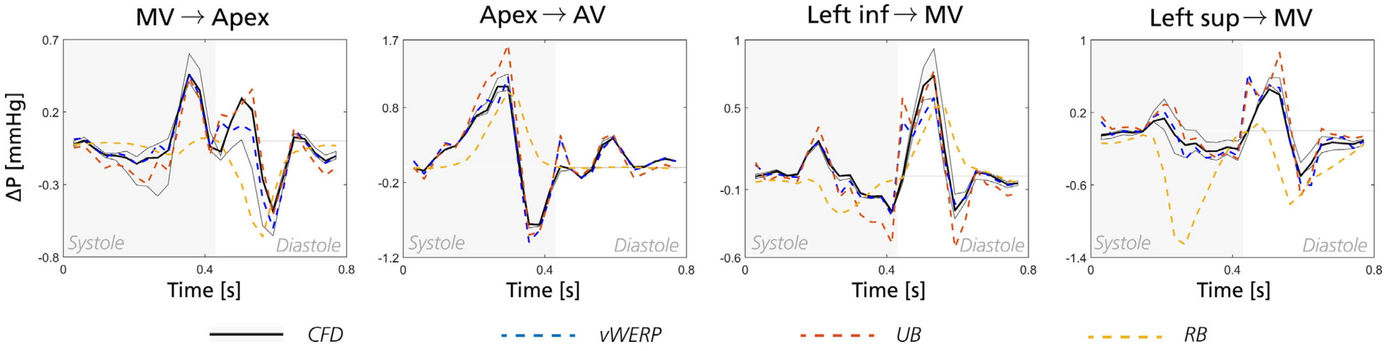

Fig. 6. Results from the patient-specific left heart model, given for four different intracardiac sections at SNR = ∞ in both left ventricle (LV) and left atrium (LA): from the mitral valve (MV) plane to a distal apical plane (first from left), from a distal apical plane to the aortic valve plane (second from left), from the left inferior pulmonary vein opening to the MV plane (third from left), and from the left superior pulmonary vein opening to the mitral valve plane (fourth from left). Relative pressure estimates are given for νWERP using a DDI approach (blue dashed), UB (red dashed), DB (yellow dashed), along with the true estimate given by voxelized equivalents of the CFD pressure field generated at the identical spatiotemporal sampling (black solid). In all instances, relative pressure is presented from systole (0 s → 0.43 s) to diastole (0.43 s → 0.8 s). (For interpretation of the references to colour in this figure legend, the reader is referred to the web version of this article.)

Table 2
Numerical data for the noise sensitivity analysis, performed on pressure drop assessment between the mitral valve plane and an apical plane in the patient-specific left heart model. Results are presented for four different pressure drop assessment methods (from left to right: νWERP with DDI, νWERP with SDI, UB, and RB), with output given for normalized Fréchet distance d_f and the errors at peak positive ($\varepsilon(\Delta P_{\max})$) and peak negative ($\varepsilon(\Delta P_{\min})$) relative pressure, respectively. Data are in all instances given in %.

	νWERP - DDI			νWERP - SDI			UB			RB		
SNR	d_f	$\varepsilon(\Delta P_{\max})$	$\varepsilon(\Delta P_{\min})$	d_f	$\varepsilon(\Delta P_{\max})$	$\varepsilon(\Delta P_{\min})$	d_f	$\varepsilon(\Delta P_{\max})$	$\varepsilon(\Delta P_{\min})$	d_f	$\varepsilon(\Delta P_{\max})$	$\varepsilon(\Delta P_{\min})$
∞	14.3	0.7	8.7	13.5	8.6	11.0	28.4	4.5	4.8	90.1	105.3	21.8
25	14.3 ± 1.0	1.4 ± 0.9	8.8 ± 1.2	13.8 ± 1.1	8.2 ± 1.3	10.9 ± 1.4	34.8 ± 9.7	10.9 ± 7.4	11.8 ± 11.5	89.4 ± 0.9	104.8 ± 1.3	18.2 ± 5.6
15	14.4 ± 1.7	2.0 ± 1.2	9.0 ± 2.0	14.1 ± 1.9	7.7 ± 2.1	11.3 ± 2.3	44.5 ± 16.3	16.5 ± 12.1	16.5 ± 19.1	89.4 ± 1.5	105.1 ± 1.9	15.3 ± 6.0
5	17.4 ± 4.0	7.2 ± 4.1	13.2 ± 6.2	19.8 ± 4.8	4.8 ± 4.4	15.8 ± 7.4	103.6 ± 50.6	46.5 ± 36.5	46.2 ± 57.9	106.0 ± 12.3	120.4 ± 9.1	17.7 ± 15.5

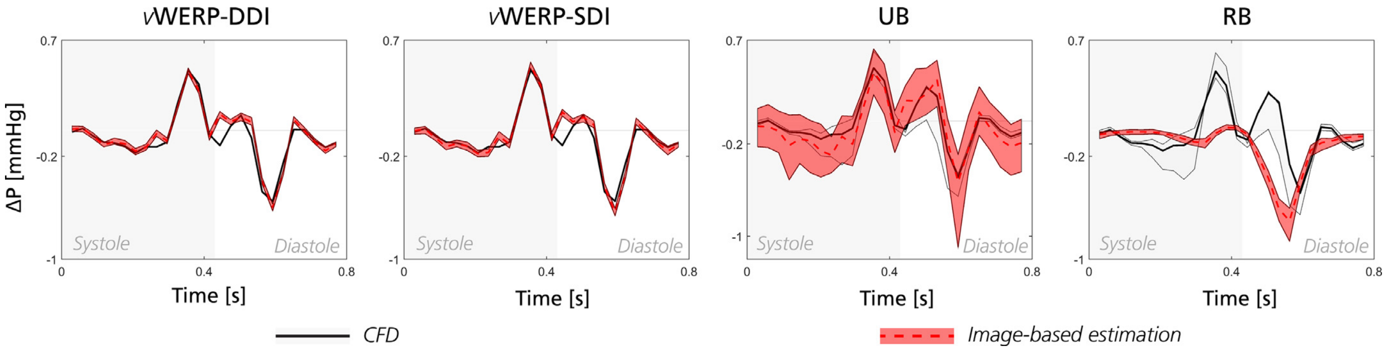

Fig. 7. Results from the patient-specific left heart model, given for assessment from the MV plane to a distal apical plane in the LV. Output shown as part of the noise sensitivity study, with data shown for νWERP using a DDI and SDI approach (first and second from left), UB (third from left) and RB (fourth from left, respectively). In all instances, output from 50 samples at SNR = 15 is shown (red shaded area, mean output as red dashed) together with comparative data from voxelized equivalents of the CFD pressure field, generated at the identical spatiotemporal sampling: for νWERP comparisons are given against the mean pressure drop between Γ_i and Γ_o (black solid line), for UB and RB comparisons are given against a Γ_i mid-point Γ_o to mid-point pressure drop (black solid line) as well as an area showing the range of possible pressure differences between any two points at Γ_i and Γ_o (gray shaded area). In all instances, relative pressure is presented from systole (0 s → 0.43 s) to diastole (0.43 s → 0.8 s). (For interpretation of the references to colour in this figure legend, the reader is referred to the web version of this article.)

νWERP DDI approach indicates slightly higher accuracy (at SNR = 15, $\varepsilon(\Delta P_{\max}) = 2.0 \pm 1.2$ for DDI vs. 7.7 ± 2.1% for SDI, respectively). The difference, however, diminished with increasing image noise (at SNR = 5, $\varepsilon(\Delta P_{\max}) = 7.2 \pm 4.1$% for DDI, vs. 4.8 ± 4.4% for SDI).

For the alternative Bernoulli-based approaches, at the noise-free configuration UB estimates are providing fairly accurate estimates, whereas RB show decreasing accuracy with the method not able to capture the transient behavior of the true intraventricular pressure drop, as evident in Fig. 7. Furthermore, both UB and RB deteriorate with increasing noise level. For UB, estimates in the high-noise scenario (SNR = 5) exhibit $d_f = 103.6 \pm 50.6$, and RB exhibit similar output deterioration with $d_f = 106.0 \pm 12.3$. In both instances, the estimates of peak pressure drops are similarly affected by added image noise.

3.2.3. Effect of sub-domain extent

To show the effect of eroding or dilating domain extent on the νWERP SDI approach, results are presented in Table 3.

Both erosion and dilation of the SDI sub-domain Ω_s affects νWERP output, however to different extents. In the case of sub-domain erosion (removal of outer-most layers of Ω_s) accuracy does not change substantially from the non-eroded SDI results in Table 2, and at a noise-free configuration the difference in d_f between a non-eroded and a four-layer eroded configuration is virtually negligible (d_f varying within 1.5% over all erosion tests). With

Table 3
Numerical data for the sub-domain extent analysis, performed on pressure drop assessment between the mitral valve plane and an apical plane in the patient-specific left heart model. Results are presented for νWERP using the SDI approach, however modifying the initial SDI domain Ω_s by either *eroding* (removing the outermost layer of Ω_s, top), or *dilating* (adding an outer layer onto Ω_s, bottom) the domain. In both instances, erosion or dilation is performed from 1 to 4 layers. Output is presented for mean error ε_{mean} and the errors at peak positive ($\varepsilon(\Delta P_{\max})$) and peak negative ($\varepsilon(\Delta P_{\min})$) relative pressure, respectively. Data are in all instances given in %.

	Erosion - 1 layer			Erosion - 2 layers			Erosion - 3 layers			Erosion - 4 layers		
SNR	d_f	$\varepsilon(\Delta P_{\max})$	$\varepsilon(\Delta P_{\min})$	d_f	$\varepsilon(\Delta P_{\max})$	$\varepsilon(\Delta P_{\min})$	d_f	$\varepsilon(\Delta P_{\max})$	$\varepsilon(\Delta P_{\min})$	d_f	$\varepsilon(\Delta P_{\max})$	$\varepsilon(\Delta P_{\min})$
∞	13.2	2.9	1.4	13.7	3.4	1.8	12.2	5.9	1.5	13.5	9.4	3.9
25	13.3 ± 0.9	3.4 ± 1.4	1.5 ± 1.1	13.9 ± 1.7	4.0 ± 1.6	2.0 ± 1.4	12.3 ± 1.7	6.1 ± 2.1	1.9 ± 1.5	13.9 ± 2.5	9.7 ± 3.2	4.3 ± 2.4
15	13.7 ± 1.6	4.0 ± 1.9	2.1 ± 1.6	14.4 ± 2.6	4.5 ± 2.5	2.6 ± 2.0	12.7 ± 2.7	6.2 ± 3.2	2.8 ± 2.1	15.1 ± 3.6	9.9 ± 5.0	5.5 ± 3.5
5	16.2 ± 4.0	7.7 ± 5.5	5.7 ± 4.7	19.0 ± 5.6	8.9 ± 6.3	6.9 ± 5.5	20.2 ± 4.9	9.4 ± 7.1	7.8 ± 6.0	29.6 ± 7.8	14.7 ± 10.6	14.3 ± 10.6
	Dilation - 1 layer			Dilation - 2 layers			Dilation - 3 layers			Dilation - 4 layers		
SNR	d_f	$\varepsilon(\Delta P_{\max})$	$\varepsilon(\Delta P_{\min})$	d_f	$\varepsilon(\Delta P_{\max})$	$\varepsilon(\Delta P_{\min})$	d_f	$\varepsilon(\Delta P_{\max})$	$\varepsilon(\Delta P_{\min})$	d_f	$\varepsilon(\Delta P_{\max})$	$\varepsilon(\Delta P_{\min})$
∞	21.9	0.4	8.9	59.2	49.6	59.2	64.7	60.2	64.7	71.7	72.9	71.7
25	21.9 ± 1.0	0.9 ± 0.8	8.3 ± 1.5	57.5 ± 3.2	49.1 ± 1.6	57.5 ± 3.2	62.5 ± 3.8	59.7 ± 1.6	62.5 ± 3.8	69.3 ± 4.0	72.5 ± 1.6	69.3 ± 4.0
15	21.6 ± 1.4	1.3 ± 1.2	8.4 ± 2.3	57.5 ± 4.1	49.0 ± 2.4	57.5 ± 4.1	62.5 ± 4.5	59.6 ± 2.4	62.5 ± 4.5	69.3 ± 4.5	72.4 ± 2.5	69.3 ± 4.6
5	20.6 ± 3.1	3.7 ± 3.6	9.4 ± 6.0	58.3 ± 9.2	48.5 ± 7.0	58.8 ± 9.7	63.5 ± 8.9	59.2 ± 7.0	63.0 ± 9.6	70.2 ± 8.3	71.9 ± 7.2	69.5 ± 9.3

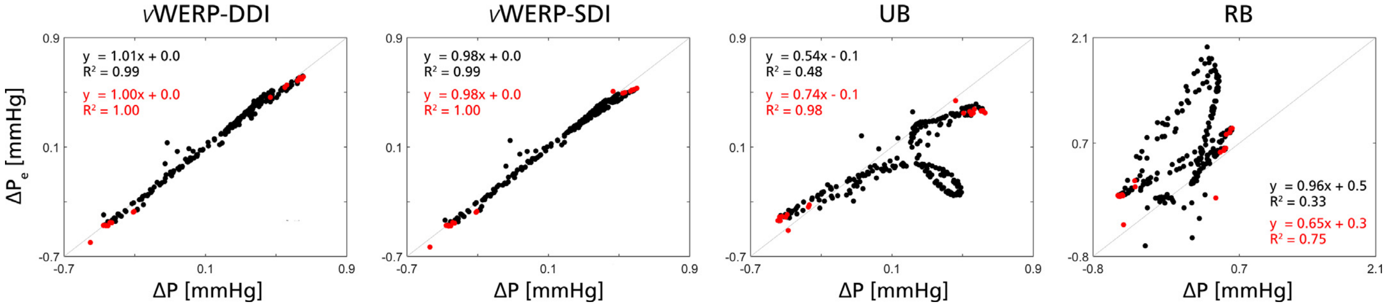

Fig. 8. Linear correlation plots for the evaluation of relative pressure through the dynamic domain benchmark problem and the patient-specific left heart model, together. True relative pressures are given as ΔP, with estimates provided by ΔP_e. Values and correlations for peak true relative pressure only, are shown in red. Plots are shown, from left to right, for νWERP using a DDI approach, νWERP using a SDI approach, UB, and RB, respectively. Note that to make the two combined *in-silico* settings comparable, data is only shown for spatial sampling of 1–2 mm^3, at SNR = ∞. (For interpretation of the references to colour in this figure legend, the reader is referred to the web version of this article.)

increasing noise, the overall d_f varies slightly more. In particular, the higher the degree of erosion, the higher the variation in output becomes (at SNR = 5, d_f = 16.3 ± 4.0% at one-layer erosion, vs. 29.6 ± 7.8% at four-layer erosion). The effect is also notable for the errors at peak relative pressure, however, the effect is within ±10% or 0.1± mmHg, and slight variations might be attributed to noise-induced fluctuations at discrete time points.

On the other hand, for sub-domain dilation (addition of outermost layers onto Ω_s) results are more significantly affected. In particular, for two-layer dilation and onward, a distinct decrease in accuracy is observed, with d_f reaching values of over 70%. The effect on the peak pressure drop assessment is particularly evident at the largest four-layer dilation, for which $\varepsilon(\Delta P_{\max})$ and $\varepsilon(\Delta P_{\min})$ = 72.9 and 71.7% at SNR = ∞, respectively. However, in comparison to the domain erosion, domain dilation is not as substantially affected by image noise and instead behaves similarly to the non-dilated, non-eroded, original SDI approach in Table 2 over all evaluated noise levels.

3.3. Cumulative analysis of validation for intracardiac relative pressure assessment

Fig. 8 shows linear regression plots for estimated vs. true relative pressure, given for all evaluated cases in Section 3.1–3.2 (data shown only for 1–2 mm^3 data, at SNR = ∞). Bland-Altman plots of the same data are presented in Fig. 9. Note that in both instances, values for peak relative pressures are given in red.

As evident in Fig. 8, both νWERP approaches show excellent accuracy, with an almost 1:1 relationship observed to the true relative pressure data (linear regression slope k = 1.01 and 0.98 for DDI and SDI, respectively). The accuracy is also observed in the Bland-Altman analysis, with both approaches rendering a mean error of 0 ± 0.03 mmHg for DDI, and -0.01 ± 0.03 mmHg for SDI, respectively. Similar values are reported for peak relative pressures.

For the alternative Bernoulli estimates, UB shows a linear regression slope of k = 0.54 and R^2 = 0.48, indicating deteriorating estimation accuracy. Slightly better output is observed at peak relative pressures (k = 0.74, R^2 = 0.98), however deviation from a 1:1 relationship remains. These results are also corroborated by the Bland-Altman data, showing a slight underestimation bias, with a mean error of -0.17 ± 0.24 mmHg. Still, the underestimation is less pronounced at peak relative pressures (-0.06 ± 0.15 mmHg).

RB shows a stronger deterioration, with a linear regression slope of k = 0.96 however with R^2 = 0.33, and with a visually apparent deviation from an true 1:1 relationship seen in Fig. 8. The Bland-Altman analysis further underlines this, with a mean error of 0.44 ± 0.45 mmHg, and even at peak relative pressure the deviation from true data seem apparent (k = 0.65, R^2 = 0.75, bias of 0.29 ± 0.27 mmHg).

3.4. Intraventricular pressure drops from 4D flow MRI

For the assessment of intraventricular relative pressure from *in-vivo* 4D Flow MRI data, results are presented in Figs. 10–11.

For the pressure drop from the MV to an apical plane (Fig. 10), νWERP indicates an initial systolic negative pressure drop of -1.6 to -4.7 mmHg, with no visible difference between healthy subjects (systolic peak at -3.1 ± 1.2 mmHg) and the patient with impaired relaxation (systolic peak at -3.1 mmHg). However, during diastole the differences become more pronounced. For the healthy subjects, two separate, negative pressure drops can be observed, corresponding to the E- and A-wave inflow shown in the flow traces

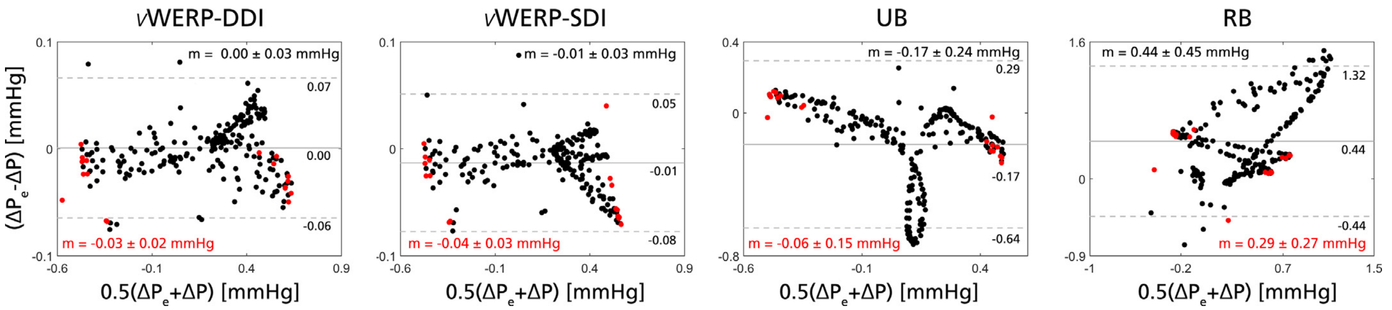

Fig. 9. Bland-Altman plots for the evaluation of relative pressure through the dynamic domain benchmark problem and the patient-specific left heart model, together. True relative pressures are given as ΔP, with estimates provided by ΔP_e. Values and bias at peak true relative pressure only, are shown in red. Plots are shown, from left to right, for νWERP using a DDI approach, νWERP using a SDI approach, UB, and RB, respectively. Note that 95% limits are indicated by the gray dashed lines, and mean ± standard deviation is explicitly given in each plot. Note further that to make the two combined *in-silico* settings comparable, data is only shown for spatial sampling of 1–2 mm^3, at SNR = ∞. (For interpretation of the references to colour in this figure legend, the reader is referred to the web version of this article.)

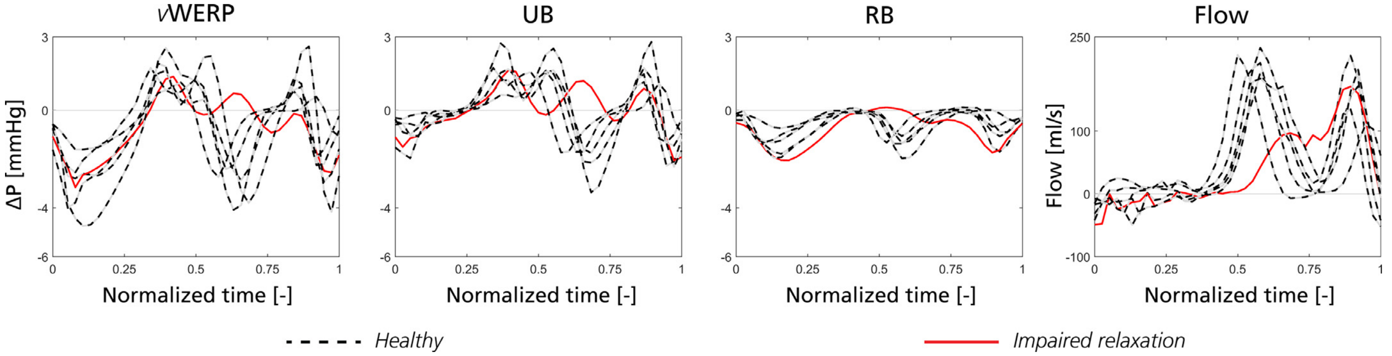

Fig. 10. Results from the *in-vivo* estimation of relative pressure (ΔP) from the MV down to an apical plane. Pressure drops are shown as derived by νWERP, UB, and RB, respectively (left to right). The five healthy subjects and the patient with impaired relaxation are given by black dashed, and a red solid line, respectively. For reference, mitral valve through-flow is given on the far right, indicating the timing of the systolic and diastolic cardiac phases (E-wave around 0.5, A-wave around 0.8). (For interpretation of the references to colour in this figure legend, the reader is referred to the web version of this article.)

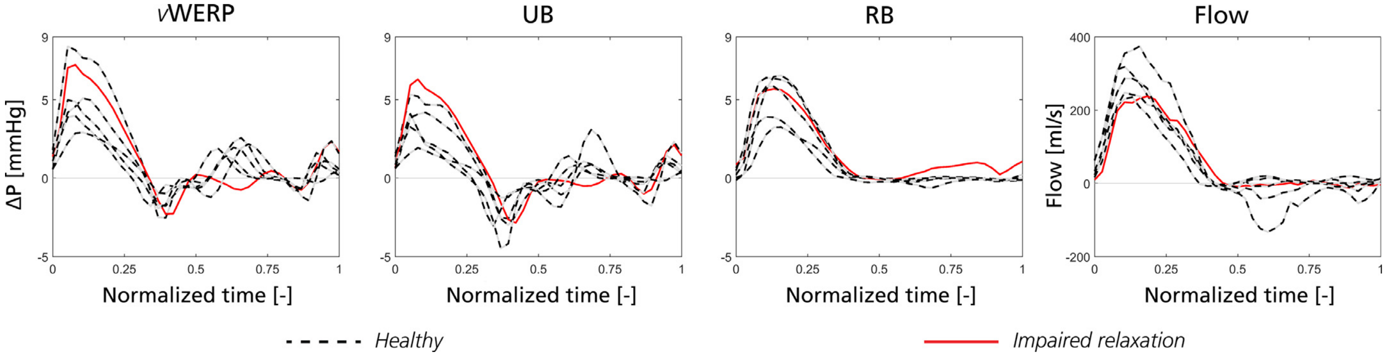

Fig. 11. Results from the *in-vivo* estimation of relative pressure (ΔP) from an apical plane up to the AV. Pressure drops are shown as derived by νWERP, UB, and RB, respectively (left to right). The five healthy subjects and the patient with impaired relaxation are given by black dashed, and a red solid line, respectively. For reference, aortic valve through-flow is given on the far right, indicating the timing of the systolic and diastolic cardiac phases. (For interpretation of the references to colour in this figure legend, the reader is referred to the web version of this article.)

to the far right in Fig. 10 (E-wave relating to early diastolic filling and ventricular relaxation, around 0.5 in normalized time in 10, A-wave relating to atrial contractoin, around 0.8 in normalized time in Fig. 10). During E-wave, the healthy subjects show a negative pressure drop of -3.2 ± 0.7 mmHg, subsequently recovering to an effective zero pressure drop state, before returning to a negative pressure drop of -2.5 ± 1.2 mmHg during A-wave. For the impaired relaxation patient, however, an apparent absence of E-wave pressure drop can be observed, with mere fluctuations around an effective zero-level seen throughout (coupled to the altered mitral plane through-flow, to the far right in Fig. 10). Only during late diastole and at the end of the A-wave inflow does any observable negative pressure drop return, peaking at -2.6 mmHg.

For the alternative approaches, UB shows an almost complete absence of systolic events, however, with some indicated E- and A-wave behaviour during diastole. Specifically, using the UB approach, the healthy subjects exhibited a negative pressure drop of -2.1 ± 0.7 mmHg at E-wave, and -1.7 ± 0.6 mmHg at A-wave, compared to no E-wave pressure drop, and -2.1 mmHg A-wave pressure drop, for the impaired relaxation patient. For the RB, even further dampening of derived relative pressure is observed during diastole, with only minor peaks appearing at E- and A-wave respectively. During systole, indications of increased relative pressure is observed, however without any differences inferrable between healthy subjects (systolic peak at -1.4 ± 0.5 mmHg) and the impaired relaxation patient (systolic peak at -2.1 mmHg).

Continuing with data from an apical plane to the aortic outlet (Fig. 11), νWERP shows a distinct positive pressure drop during systole, being similar in magnitude between the healthy subjects (4.2 ± 1.0 mmHg) and the impaired relaxation patient (7.2 mmHg). During diastole, early E-wave positive pressure drops can be observed for the healthy subjects (1.8 ± 0.3 mmHg), however, seem absent in the diseased patient. During A-wave and late diastole, slightly dampened pressure drops are observed, however in this instance similar between healthy subjects (1.2 ± 0.8 mmHg) and the diseased patient (2.3 mmHg). For the apical plane to aortic outlet assessment, both UB and RB indicate positive systolic pressure drops in both healthy and diseased subjects. For both UB and RB, similar magnitude are observed between the impaired relazation patient and the healthy subject cohort (UB showing a systolic peak at 3.8 ± 1.3 mmHg in healthy, 6.3 mmHg in diseased, RB showing a systolic peak at 5.2 ± 1.5 mmHg in healthy, 5.7 mmHg in diseased).

4. Discussion

In this study, we have presented an extension of the virtual work energy method, νWERP, designed to handle dynamic domains and specifically tailored for intracardiac flow assessment. By solving a virtual work-energy balance on a sub-domain problem, we show that accurate estimates of relative pressure can be achieved, validating output *in-silico*, as well as indicating diagnostic abilities *in-vivo*. With νWERP outperforming alternative estimation techniques, the method promises refined assessment of intracardiac relative pressure.

4.1. Evaluation and validation of νWERP performance

For all evaluated *in-silico* datasets, νWERP showed excellent accuracy, with an almost 1:1 relationship indicated against true relative pressure ($k = 1.01$ and 0.99, $R^2 = 0.99$ and 0.99 for DDI and SDI approaches, respectively). From the Bland-Altman plots in Fig. 9, a small tendency towards increasing deviation with increasing absolute pressure drops can be observed, however average deviations are within 0 ± 0.04 mmHg for all evaluated cases.

In Section 3.1, the dynamic domain benchmark problem was utilized to map νWERP performance over ranges of spatiotemporal image sampling, with generally excellent output reported (average $d_f = 16.0\%$, corresponding to an absolute error below 0.05 mmHg). As briefly noted, a minor favoring of temporal over spatial refinement seems apparent, even though at finer temporal scales spatial dependence seem slightly more dominant. Noteworthy is that strict improvement is not apparent at the very coarsest spatial resolutions of the dynamic domain benchmark problem (going from 4 to 3 mm^3). This is most likely a result of the complex flow field being represented by an overly coarse grid, and where domain boundaries are slightly differently represented at the two resolutions due to the indivisible match between 3 and 4 mm^3 grids. If instead following a traditional convergence rate (using divisible voxel splitting, going from 4 to 2 mm^3, and 2 to 1 mm^3) more steady convergence is observed.

Regardless, fairly low errors reported throughout, and differences in error between increased temporal vs. increased spatial sampling are within 5–10%. As such, the appropriate choice of spatiotemporal sampling might instead depend on the physical nature of the evaluated clinical case: if assessing narrow intracardiac spaces where flow is governed by advective motion (such as the outflow tract of an obstructive hypertrophic cardiomyopathy patient), one might opt for improved spatial sampling. Conversely, if assessing transient cardiac events where flow is governed by kinetic motion (such as rapid filling or early ejection), preference might instead be on temporal sampling. Such consideration, and confirmation of these trends, might however have to be decided as a function of evaluated disease type. Here, it should also be noted that evaluations at the coarsest most temporal sampling (50 ms) showed an apparent increase in estimated output error. 40–50 ms temporal sampling is not uncommon for clinical cardiac 4D Flow MRI, and as such, increased spatial sampling might be recommended to compensate for the lack of temporal accuracy. However, even though indicating highest d_f, absolute errors in relative pressure at 50 ms were still below 0.1 mmHg. Further, with contemporary acceleration techniques promising improved temporal resolution (Jung et al., 2011; Giese et al., 2014), this might not be an inherent clinical drawback to the presented νWERP approach.

Continuing, the patient-specific left heart model was used to validate νWERP in a realistic flow scenario, as well as to specifically map output over different level of image noise. As reported in Table 2, νWERP exhibits stable performance over all evaluated noise levels, in part following from its integrative nature. Here, the consistently high accuracy also showcases how the complete fluid mechanical description utilized by νWERP - including kinetic, advective, and viscous flow components in the formulated virtual work-energy balance - sufficiently captures the flow features encountered within the intracardiac space.

4.2. Alternative estimation techniques and comparative performance

In addition to the evaluation of νWERP performance, relative pressure was also derived using an RB and a UB formulation; both representing clinically utilized methods. As indicated, varying output was reported for the two approaches.

4.2.1. Unsteady bernoulli and intracardiac flow

For UB, linear correlation output shows distinct deviation from true relative pressure ($k = 0.54$, $R^2 = 0.48$), with output accuracy decreasing with increasing relative pressure - notably with the main decrease in accuracy coming from the dynamic domain benchmark problem (see Fig. 5). The Bland-Altman plot in Fig. 9 also indicates a slight underestimation bias (in average, -0.17 ± 0.24 mmHg), even at peak relative pressures. In particular, UB shows increasing deviation with increasing image noise, where results in Table 2 show how at high-noise (SNR = 5), UB output increases to $d_f = 103.6 \pm 50.6\%$. The reason for all of this behavior can be explained by appreciating the nature of the method and how it is used.

The expression given in Eq. (25) is derived from the Navier-Stokes equations, assuming negligible viscous impact, and further reducing the evaluation of relative pressure to assessments along an integration line connecting Γ_i and Γ_o, with velocity data projected in the direction of this selected path. In strict theoretical terms, this formulation only holds for an integration line that follows the physical path or instantaneous streamline of an arbitrary particle sampled into the assessed flow field (Segletes and Walters, 2002). In practice, however, extracting a physical particle streamline requires access to accurate full-field data, and is a comparably data heavy approach. Instead, a user-defined integration line is often selected to represent the evaluated path (as also used in Eq. (25), in conventional practice, and throughout our assessments). This is not only a practical choice, but works well if assessing unidirectional flow along a dominant jet structure, as supported by the well-captured peak pressure drops in Fig. 6. Similarly this explains the fairly well-coinciding output between νWERP and UB in assessing early diastolic filling through the MV (Fig. 10), as well as in systolic ejection towards the AV (Fig. 11). However, in phases of non-unidirectional flow, or if assessing pressure drops in directions that are non-aligned with dominant flow features, the choice of a linear integration path will no longer validly represent a true physical streamline. Furthermore, the projection of data in the direction of the integration line will mean that only a portion of the true field is taken into account, when flow is non-aligned with this interrogation direction. With intracardiac flow characterized by transiently varying, complex flow features (Töger et al., 2012; van der Geest and Garg, 2016), the assumptions made by a UB assessment might thus vary in validity over the cardiac cycle: a fact corroborated by the UB output given in the *in-silico* validations where UB accuracy varies over time. Similarly in the *in-vivo* evaluation, UB systolic pressure drop is seemingly absent in MV to apex assessment (Fig. 10) - a phase where flow is not co-aligned with the selected integration line going from mid-MV to apex.

Re-iterating, the issues surrounding the UB approach can be divided into two parts: *A)* that velocities used - in particular for the advective part of UB - are projected in the direction of a selected integration line, and *B)* that the selected integration line might not represent a physical instantaneous streamline. For *A)*, this choice of velocity projection is typically done in conjunction to Doppler-based evaluations, where the nature of the ultrasound acquisition restricts assessments to velocity components aligned with the interrogating ultrasound beam (Firstenberg et al., 2000; Yotti et al., 2004; 2005). This does not limit the assessment of the inertial component of Eq. (25) (where data is - by definition - projected along the integration line), however does restrict accuracy with respect to the advective part. In the instance of 4D Flow MRI, full-field data is readily available and such velocity projection is not necessary (Ebbers et al., 2001). In fact - as expanded upon in Appendix D - when including the *complete* velocity field in the evaluation of the advective momentum drop of Eq. (25), a distinct increase in method accuracy is observed for the evaluated *in-silico* cases. Specifically, for the dynamic domain benchmark problem, when incorporating the complete velocity field into the UB evaluation, average d_f decreases from 95.2% to 33.5% (see Appendix Table D.1). Similarly, the deviation from true relative pressure seen in Fig. 8 diminishes when avoiding velocity projections (see Supplementary Fig. D.1). It should however be stressed that this represents a non-conventional usage of the UB approach given in Eq. (25).

Secondly for *B)*, the main issue with replacing a physical streamline with a user-defined integration line, is that the selected line direction is not always aligned with the direction of the real, assessed flow. With a step-by-step theoretical description again provided in Appendix D, this can be overcome by avoiding to simplify the advective component into a squared magnitude difference (as per Eq. (25)), and instead derive relative pressure from a full Euler form of the UB approach. Here, the reason to why a full Euler UB expression is not considered a standard UB form, is that in the absence of full-field data, the spatial gradient of $\mathbf{v}$ - required for a full Euler UB formulation - is typically unknown. Using 4D Flow MRI, spatial gradients are though readily available. In fact, in addition to the improvements observed with avoiding velocity projections, further incremental improvement is observed when using a full Euler form of UB. Over the dynamic domain benchmark problem, average d_f decreases further to 24.7%. As such, accurate output can be achieved by UB, although the observed behavior underlines practical difficulties in using UB with projected velocity components and user-defined integration lines. Similarly, the variation in output speaks to the user-dependency of UB, which - in comparison to νWERP - yields potential variation dependent on user selected points. Summarizing, UB might thus still have potential in the intracardiac space, however dedicated, separate studies are required to clarify specific variations and data processing strategies tailored for this application area.

Importantly, a final observation of the UB approach is its noise dependency, where significant deviations were indicated at increasing image noise ($d_f = 103.6 \pm 50.6\%$ at SNR = 5), as well as its dependence on the selected inlet and outlet points $\mathbf{q_i}$ and $\mathbf{q_o}$ (rendering the variation in estimated output shown by the gray shaded areas in Figs. 5–7). In both of these instances, the behavior can be explained by the reduction of data to a user-defined integration line: in comparison to νWERP where output is generated by integrating over an entire defined sub-domain, UB will rely only on the image voxels given along this specified line. Consequently, the method becomes much more prone to spurious image noise, rendering - as indicated in the *in-silico* tests - higher errors under evaluated, realistic acquisition scenarios. Importantly, this noise-dependency will be evident regardless of theoretical approach (utilizing projected velocities, full-field data, or an irrotational UB form), representing a drawback of UB as compared to the full-field equivalent of νWERP.

4.2.2. Reduced bernoulli and intracardiac flow

In comparison to both νWERP and UB, the RB shows higher deviations to true pressure data, and d_f is frequently above 80% over all evaluated tests. Likewise, no apparent convergence is observed in Table 1, stemming from the fact that RB assumes flow being governed by peak velocities, which - in instances of complex flow fields - causes method deterioration as higher velocities are being resolved. Importantly, the method is also not particularly designed to capture temporal variations in relative pressure, as seen in Figs. 5–7, where temporal mis-alignments seem visually apparent. Here, the principal drawback comes from the fact that RB assumes relative pressure being exclusively governed by advective accelerations, and that flow can be further assumed as unidirectional. Albeit this assumption holds for a subset of intracardiac flow scenarios (such as around severe outflow tract obstruction, or over high-magnitude flow valvular stenosis), this cannot be held valid for broader intracardiac assessments. Importantly, even when assessing instantaneous pressure drops over stenosed valve openings - a hemodynamic scenario where RB assumptions could be viewed as sensible - indications of method bias are frequently reported (Baumgartner et al., 1999; Feldman and Guerrero, 2016; Donati et al., 2017). Separate, dedicated studies might again help specify data processing steps to improve RB estimates, however, such goes beyond the scope of this current work.

4.3. Comparative performance and implications of dynamic vs. static sub-domains

In all of the above presented sections, the extended νWERP approach was evaluated using both a DDI and an SDI approach. As given in Section 2.3, the two both rely on the concept of solving νWERP on a defined sub-domain, however, where the DDI approach generates dynamically updated Ω_s from the intersect of consecutive image frames, the SDI approach will utilize a smaller Ω_s generated as the complete intersect over *all* existing image frames.

Even though different in its practical implementation, both are equally valid thanks to the fact that the posed virtual work-energy balance holds on any arbitrarily chosen sub-domain. The results from our evaluations also corroborate this: in the dynamic domain benchmark problem the difference between DDI and SDI output is almost negligible, and in the patient-specific left heart model only minor preference is indicated for the static, SDI approach (SDI showing in average 0.2% lower d_f compared to DDI).

Thus, the choice between a DDI or an SDI approach will be governed by practical rather than theoretical considerations. As noted in Section 2.3, any choice of sub-domain approach will inherently decrease the number of data points included in the νWERP computation. Herein, the DDI approach will maximize utilized data, whereas the SDI approach will be limited to the global intersect over all time frames. Thus, if assessing a dynamic domain with significant translational motion, and where there is no joint intersect union (i.e. $\Omega_s = \Omega(t_0) \cap \Omega(t_1) \cap \Omega(t_2) \cap \ldots \cap \Omega(t_n) = \emptyset$), SDI will no longer be applicable. Similarly, even if $\Omega_s \neq \emptyset$, a reduction in sub-domain extent might make SDI more sensitive to local fluctuations in data quality. For the sake of intracardiac assessments, excessive translational motion is not of any major concern (Arts et al., 1992), however volumetric changes of over 50% are routinely encountered in the ventricles. As such, the choice of DDI vs. SDI could be made based on probed intracardiac space: physiological movements in and around the atrioventricular plane will make assessment of MV behavior more suited for a DDI-approach, whereas assessment in and around the more anchored apical end might make SDI a viable candidate. Nevertheless, with interchangeable DDI vs. SDI output indicated in the dynamic domain benchmark problem (where volumetric changes are up to 46%), and with neither of the approaches overly affected by image noise in the patient-specific left heart model, the two approach could possibly be seen as identical for the sake of output accuracy when assessing pressure drops through entire cardiac chambers.

Lastly, a minor practical benefit exists with the SDI approach. Here, the static nature of the defined Ω_s means that a single virtual field $\mathbf{w}$ holds over all time frames, and Eqs. (11)–(13) will only have to be solved once for a given cardiac cycle. Conversely, in the DDI approach, $\mathbf{w}$ has to be continuously re-calculated, and Eqs. (11)–(13) have to be separately solved for each updated definition of Ω_s. To exemplify, in the patient-specific left heart model a νWERP SDI assessment is completed in about 20 s, whereas a DDI equivalent - with $\mathbf{w}$ solved separately for each 27 time frames - requires about 7 minutes. With increasing computational power, this discrepancy might diminish as the νWERP process is trivially parallelizable in time, however, for increasing domain sizes, SDI might represent a more practical implementation.

4.4. Effect of sub-domain extent

In Section 3.2.3, the effect of sub-domain extent on νWERP SDI output was evaluated, achieved by iteratively eroding or dilating the initial Ω_s, given by Eq. (20). As reported, eroding the domain and effectively creating a more conservative, smaller Ω_s did only impact output slightly, with d_f remaining at around 15% for most levels of evaluated erosion. Conversely, however, dilating the sub-domain and effectively creating a Ω_s being *larger* than the dynamic domain Ω had a significant negative impact on output accuracy.

This is an interesting finding, but has a natural explanation when acknowledging the theoretical derivation of νWERP. In Section 2.1, the virtual work-energy components in Eqs. (4)–(8) are derived by converting the Navier-Stokes equation into a work-energy balance, and integrating over the fluid domain Ω. Herein, pressure p is extracted from the virtual input hydraulic power component $H(p)$, using integration by parts. Similarly, simplifications of V_e and S_e are arrived at applying integration by parts. This manipulation is allowable under the generally held assumption that the integrands are continuously differentiable (*e.g.* that ∇p and $\mu\nabla \cdot \nabla\mathbf{v}$ are continuously differentiable functions). This is a reasonable assumption over the domain of the fluid, but should not hold in the dilation case where the domain is larger than the true fluid, and where discontinuous jumps likely occur at the true fluid boundary. Hence, when the evaluated domain does not conform to the true flow domain, the inclusion of surrounding static tissue renders non-smooth transitions (in a physiological imaging scenario, p will exist in surrounding tissue, however, the transition from blood to tissue will be non-smooth). The issues surrounding pressure estimation over non-smooth and non-continuous arguments when performing integration by parts is also highlighted in an analytic example provided in Appendix E.

When $\Omega_s \subseteq \Omega$, $\mathbf{v}$, p and $\mathbf{w}$ are continuously and smoothly defined within Ω_s, assumptions of continuous differentiability stays valid, and νWERP estimates should hold. This is the case for both the general SDI approach, and for any given erosion of that domain. However, if Ω_s spans *beyond* Ω meaning that $\Omega_s \not\subseteq \Omega$, assumptions on continuity breaks down, and errors appear (as again exemplified in Appendix E). It is here worth noting that in the patient-specific left heart model, Ω was embedded with zero space. As such, any domain dilation would cause an inclusion of voxels where $p = 0$, representing a worst-case scenario with respect to differentiability and smoothness. Such drastic singular changes might not be present *in-vivo*, regardless, our evaluation on sub-domain extent highlight the dependency on domain definition.

In practice, this behavior does however not represent any principle limitation, but does instead highlight the benefits of νWERP: if assessing an intracardiac domain where limited acquisition quality or rapid anatomical movements complicates accurate definition of domain boundary, νWERP permits using a more conservative segmentation, where only the core of the flow domain is used to derive accurate pressure drops. That is, where other alternative approaches such as the PPE method relies more heavily on accurately resolved boundary flows (Bertoglio et al., 2018; Donati et al., 2014), νWERP only requires accurate and continuous estimates within a virtually created sub-domain. Here, the trade-off with using a smaller sub-domain is that estimates become more dependent on data quality, and that care needs to be taken to ensure convergence when solving for $\mathbf{w}$ in Eqs. (11)–(13). Whereas the latter can be handled by increasing the level of data subsampling (as outlined in Section 2.4.2), the importance of sufficient subsampling should not be overlooked: if using insufficient subsampling, $\mathbf{w}$ will not be solved to complete numerical convergence, and we can no longer ensure that the utilized field abides to the crucial properties outlined in Section 2.1 (in practice, a level of subsampling should instead be selected such that a well-converged $\mathbf{w}$ can be ensured, e.g. by assigning a user-defined residual when solving Eqs. (11)–(13)). Regarding noise, this might remain an issue for highly eroded geometries at high-noise configuration (as indicated in Table 3. However, as also shown therein, even at a 4-layer erosion (effectively shrinking the original domain by $\approx$ 84%, going from a total of $\sim$17500 to $\sim$3000 flow voxels), the normalized Fréchet distance d_f only increases by 13.4% at the high-noise configuration of SNR = 5. Instead, the choice between a more conservative or a more inclusive sub-domain should instead be based on apparent data quality and segmentation accuracy.

4.5. Clinical indications of intraventricular relative pressure assessment

In addition to the *in-silico* validation and verification, νWERP was also applied on a small cohort of subjects scanned in 4D Flow MRI. Specifically, this was performed to *(i)* verify applicability on clinical data, *(ii)* evaluate performance in a clinical setting, but also to *(iii)* infer potential signs of diagnostic differentiation using quantitative assessment of intraventricular relative pressure.

As reported, consistent output is seen between all healthy subjects, and the temporal variations in relative pressure follow similar patterns for both the MV to apex, and apex to AV evaluation, indicating robust νWERP behavior. For the healthy subjects, greatest intersubject variability is seen at peak systole, where the relative pressure from MV to apex equals -3.1 ± 1.2 mmHg, and apex to AV equals 5.1 ± 2.1 mmHg. However, similar variations can also be inferred for the flow through both MV and AV (right-most panels, Figs. 10–11), supporting the notion that the deviations seen in the νWERP-derived relative pressures are originating from physiological flow phenomena. That peak intraventricular flow events come with greater intersubject variations - even within healthy cohorts - is also corroborated by previous 4D Flow MRI studies (Eriksson et al., 2015).

The results from the healthy subjects should be contrasted to the output from the patient with impaired relaxation and associated diastolic dysfunction. As apparent in Figs. 10–11, early diastolic relative pressures are almost completely suppressed in the impaired relaxation patient (∼0.5-0.75 in normalized time, in Figs. 10–11). The behavior is supported by the delayed E-wave inflow in the right-most panel of Fig. 10, being seemingly fused with the later A-wave inflow. The output is further in-line with hemodynamic changes associated with diastolic dysfunction: reduced early diastolic acceleration seen in end-stage dilated cardiomyopathy patients (Goar et al., 1991), disturbed diastolic relaxation patterns associated with ventricular volume overload (Schannwell et al., 2002), and a loss of apically directed hemodynamic forces inferred in LV dyssynchrony patients (Arvidsson et al., 2018). As such, and even though only applied in one patient as a proof-of-principle, the results exemplify the role of intracardiac relative pressure assessment in quantifying differences between diseased and normal subjects, and does highlight the promise of the presented νWERP approach.

For alternative Bernoulli estimates, the intersubject variability in relative pressure does not increase, however the differentiation against the impaired relaxation patient is diminished. Specifically, for the MV to apex assessment, the difference between healthy subjects and the patient at peak E-wave is 3.9 mmHg for νWERP, compared to 2.1 and 1.4 mmHg for UB and RB, respectively. Further, systolic MV to apex events seem completely suppressed in the UB assessment (Fig. 10), and diastolic apex to AV events observed with νWERP seem similarly attenuated in both Bernoulli approaches (Fig. 11). Limitations with RB in complex flow fields has been highlighted in numerous previous studies (Baumgartner et al., 1999; Garcia et al., 2003; Donati et al., 2017), and in the intraventricular space, the development of diastolic vortices (Töger et al., 2012; Pedrizzetti et al., 2014) might hinder appropriate integration line definitions in UB. In combination with the increased accuracy and more robust noise sensitivity shown for νWERP *in-silico*, this underlines the advantages of νWERP compared to alternative estimates, and highlights the potential of utilizing the method for accurate quantification of intracardiac relative pressure.

4.6. Contextualizing intraventricular νWERP assessment

It is worth contrasting the νWERP-derived *in-vivo* results with previous published work on intracardiac relative pressure. In a seminal pre-clinical work, (Courtois et al., 1988) indicated pressure increase from MV to apex, and (Firstenberg et al., 2000) assessed similar transmitral pressure gradients using catheter and Doppler-based UB-estimations in humans. Here, both E- and A-wave indicate distinct pressure gradients in the apical direction, much similar to the diastolic behavior observed by νWERP in Fig. 10. Further, albeit assessed over a slight more basal section, the magnitudes of transmitral pressure drop observed in (Firstenberg et al., 2000) - being in average 4–6 mmHg - coincide with our presented data on MV to apex behavior. Continued work from the same group of authors indicate similar transient behavior, albeit with slightly lower magnitudes (Firstenberg et al., 2001; 2008).

For full-field 4D Flow MRI data, (Ebbers et al., 2002) and (Eriksson et al., 2015) both solved a PPE to extract pressure differences in the healthy LV, whereas (Thompson and McVeigh, 2003) utilized an UB approach. In all instances, apically directed E- and A-wave peaks were again observed, however with peak differences comparably lower in magnitude (∼ 1–2 mmHg). Later work on hemodynamic forces (integrating pressure gradients over the LV volume) seem to corroborate these findings (Arvidsson et al., 2018). It should however be noted that the utilized PPE approach has shown highly dependent on the definition of the assessed flow domain, with signs of an underestimation bias even in simplified *in-silico* settings (Bertoglio et al., 2018; Donati et al., 2014). Numerous works have also assessed intraventricular systolic pressure drops towards the aortic outflow tract, confirming the systolic pressure drops observed by νWERP in Fig. 11 with peak magnitudes ranging from 2 to 3 mmHg in PPE-based assessments on cardiac 4D Flow MRI with relatively low temporal resolution (Ebbers et al., 2002), going up to 6–7 mmHg using UB in more contemporary data (Buyens et al., 2005; Thompson and McVeigh, 2003; Yotti et al., 2004). Regarding relative pressure behavior in diseased ventricles, image-based assessments are more scarce. Yotti et. al. (Yotti et al., 2005) used M-mode Doppler to assess diastolic basal-to-apex pressure drops in dilated cardiomyopathy patients, indicating magnitudes of around 1.2 mmHg in these diseased ventricles; slightly suppressed as compared to our healthy volunteer data. Using 4D Flow MRI, (Eriksson et al., 2013) compared inflow characteristics between healthy subjects and patients with dilated cardiomyopathy, showing depressed E-wave but preserved A-wave behavior; in-line with the νWERP-derived reduced E-wave pressure drop in the subject with impaired relaxation (see Fig. 10). (Rovner et al., 2005) assessed transmitral pressure drops in patients with diastolic dysfunction using UB and Doppler imaging, indicating similarly depressed peak drops, and reduced diastolic pressure drops have also been inferred in patients with diastolic impairment induced by acute myocardial ischemia (Courtois et al., 1990).

Summarized, νWERP-estimates coincides with existing literature and shows promising potential in recovering realistic intracardiac relative pressure behavior *in-vivo*. Further, with νWERP invariant to the definition of inlet and outlet section, arbitrary probing of relative pressure is permitted, making previously inaccessible or unexplored domains readily available. To exemplify, this could mean quantifying changes in LA pressure, or assessing intraventricular septal-to-lateral pressure changes, where only either catheter-based evaluations or preliminary, exploratory image-based assessments have been performed so far (Fisher et al., 1998; Eriksson et al., 2015).

4.7. Limitations

In this study, the extension of νWERP into dynamic domains was validated *in-silico*, with *in-vivo* examples provided as a proof-of-concept. As such, a strict *in-vivo* validation with catheter based pressure data as reference remains to be performed. However, acquiring intracardiac pressure data in combination with full field flow imaging comes with its own set of challenges, including co-registration issues and catheter-induced flow disturbance. However, with νWERP successfully validated on aortic *in-vivo* data (Marlevi et al., 2019), with the extracted intracardiac relative pressure traces coinciding with previously reported data (Firstenberg et al., 2000; 2001; Yotti et al., 2004; Eriksson et al., 2015), and with alternative approaches showing limited performance even in idealized *in-silico* scenarios (Bertoglio et al., 2018), the herein presented extended νWERP approach has definite potential to provide improved estimates of intracardiac pressure changes in clinics.

As formulated, νWERP makes use a virtual field with predefined properties to extract virtual energy components, all contributing to the real relative pressure. Herein, the only data-based assumption is that the contribution of virtual shear power transfer, S_e, is negligible. This is based largely on the fact that $\mathbf{w} = 0$ along Γ_w, however, terms will remain at Γ_i and Γ_o. These might grow in value in instances of non-laminar flow, as sometimes encountered in the intracardiac space. However, as the term is scaled by the dynamic viscosity μ its contribution will still be comparably small. To this, even if including S_e in the data analysis performed in Section 3, the term only contributes with less than 0.1% of the total pressure drop, being magnitudes smaller than all other virtual energy components. Its impact may be more pronounced in peripheral vessels with slower flow, however, the data confirms its negligible impact in intracardiac applications, and further validates the assumption made in the method derivation.

Furthermore, as formulated, νWERP requires full field data as input for the virtual work-energy evaluation. As showcased in our study, this can be achieved by 4D Flow MRI. However, even though acquisition settings for 4D Flow MRI are part of all contemporary clinical scanners, full field acquisitions are not part of routine protocols for incoming cardiac patients. However, recent developments on accelerated 4D Flow MRI sequences promises thoracic full-field imaging in less than two minutes (Bollache et al., 2018), and increased accuracy and quantification abilities promises a cost effective use of the technique in the near future (Heydari et al., 2015). Similarly, full-field mapping by ultrasound vector flow imaging is another emerging technology, which might aid the clinical translation of full-field analysis (Correia et al., 2016; Wigen et al., 2018). An extension of νWERP into 2D flow imaging could also be envisaged (using 2D PC-MRI, ultrasound vector flow imaging (Pedersen et al., 2014), or similar), modifying the virtual work-energy balance to act on a 2D virtual field. However, such extension would have to be separately evaluated, in particular when applied on dynamic intracardiac flows.

It should also be noted that the utilized *in-silico* datasets represent idealized analogs of an *in-vivo* scan, where synthetic flow data is generated by data projection onto an image-like grid. In a clinical scenario, patient movement, respiratory motion, heart rate variability, and acquisition-related errors might all reduce data accuracy. However, as shown in this and previous studies, νWERP is fairly invariant to added, realistic image noise, in part due to its integrative nature. In case of extensive data variations, contemporary machine learning methods have been proposed with which to both de-noise and upsampla apparent resolution (Ferdian et al., 2020); something that could prove useful also for subsequent relative pressure estimation using e.g. νWERP. Alternatively, if wanting to maintain acquired data without additional de-noising, the modified νWERP-t approach - incorporating turbulent energy dissipation in the theoretical derivation in order to compensate for stochastic flow variations - could also be utilized (Marlevi et al., 2020). The performance of νWERP-t in dynamic intracardiac domains, however, remains to be investigated. Further, comparing our *in-silico* models to clinical reality, the utilized patient-specific left heart model did not include any high-magnitude pressure gradients as encountered in severe valvular stenosis (Baumgartner et al., 2017) or obstructive hypertrophic cardiomyopathy (Sigwart, 1995; Van Ooij et al., 2016). Even if constrictive high-magnitude flows might induce post-stenotic turbulence, strong intracardiac jets will result in higher SNR and improved accuracy. Previous intraaortic νWERP validations have also shown accurate output performance through high-magnitude flow jets, indicating promise even for high-magnitude intracardiac flow scenarios.

Lastly, it should be noted that the utilized *in-vivo* cohort was limited in size. However, the cohort was not assessed to infer statistical differences or identify clinically valid trends, but rather to showcase potential and evaluate the feasibility of implementing νWERP on clinically acquired patient data. Larger cohorts will have to be explored to clarify diagnostic potential, however, the results in this study indicates that νWERP could serve as a viable tool for assessing intracardiac relative pressure at high accuracy.

4.8. Clinical outlook

Hemodynamic assessments are central in cardiac diagnostics (Richter and Edelman, 2006), and a plethora of studies exist highlighting how quantitative hemodynamic assessment improve cardiac disease management (Heydari et al., 2015; De Bruyne et al., 2014; Pedrizzetti et al., 2014). Changes in intracardiac pressure gradients have been used to describe both diastolic (Courtois et al., 1988) and systolic (Pasipoularides et al., 1987) dysfunction, however the assessment of such has so far been limited to either catheterization performed during percutaneous or invasive interventions, or to a subsets of disorders where simplified method assumptions hold.

As such, the presented extension of νWERP for intracardiac assessments widens the scope of quantitative hemodynamic diagnostics, and permits established clinical biomarkers to be applied in a broader intracardiac setting. As highlighted in the *in-vivo* assessment, νWERP acts directly on imaged full-field data and the subdomain approach makes it readily available for use on clinically acquired flow images. Furthermore, being based on a complete fluid mechanical description of intracardiac blood flow - including kinetic, advective, and viscous flow behaviour - νWERP has the ability to effectively handle all types of flow events encountered in the intracardiac space: from highly transient flows during early filling or ejection, to more subtle variations experienced during later phases.

With quantitative flow assessment providing novel insights into cardiac disease manifestations (Heydari et al., 2015; Eriksson et al., 2015; Zajac et al., 2015; Corrado et al., 2019), the herein presented extension of νWERP shows particular promise for improved clinical evaluation. Using a combination of advanced full-field imaging with a physics-based fluid mechanical description of intracardiac blood flow, νWERP permits for accurate and robust estimation of intracardiac relative pressure *in-vivo*.

5. Conclusion

We have presented an extension of the νWERP formulation, allowing for accurate assessment of relative pressure through dynamically shifting flow domains, being specifically tailored for intracardiac assessments. With relative pressure being a recognized marker for pathological cardiac developments, νWERP shows promising potential, performing favourable to alternative approaches and enabling arbitrary probing of the intracardiac space. With continued clinical validation, νWERP is poised to serve as a powerful tool for refined intracardiac diagnostics.

Author Statement

D.M. and D.N. conceived of the study and the method. The dynamic domain benchmark problem was designed by M.B., D.M., and D.N. and solved by M.B. The patient-specific left heart model was created, solved, and prepared for analysis by A.H., A.d.V, and D.F. The in-vivo data was acquired and processed by F.V., J.E., and T.E. Clinical data input was provided by N.S.B., F.D.P., J.E., and E.R.E. Data analysis was performed by D.M., with input from D.N., T.E., and P.L. D.M. write the manuscript with input from all authors. All authors approved of the final manuscript.

Declaration of Competing Interest

The authors declare that they have no competing financial interests or personal relationships that could have appeared to influence the work reported in this paper.

Acknowledgments

D.M. holds a Knut and Alice Wallenberg Foundation scholarship for postdoctoral studies at Massachusetts Institute of Technology. M.B. acknowledges funding from King's College London and Imperical College London ESPRC Centre for Doctoral Training in Medical Imaging (EP/L015226/1). D.N. would like to acknowledge funding from Engineering and Physical Sciences Research Council

(EP/N011554/1 and EP/R003866/1). P.L. holds a Wellcome Trust Senior Research Fellowship (g.a. 209450/Z/17/Z). T.E. would like to acknowledge funding from the Swedish Research Council (2018–04454) and the Swedish Heart-Lung Foundation (2018-0657). This work was also supported by the Wellcome ESPRC Centre for Medical Engineering at King's College London (WT 203148/Z/16/Z) and the British Heart Foundation (TG/17/3/33406). E.R.E. was funded in part by NIH R01 49039.

Supplementary material

Supplementary material associated with this article can be found, in the online version, at doi:10.1016/j.media.2020.101948.

References

Allen, B.D., Choudhury, L., Barker, A.J., Van Ooij, P., Collins, J.D., Bonow, R.O., Carr, J.C., Markl, M., 2015. Three-dimensional haemodynamics in patients with obstructive and non-obstructive hypertrophic cardiomyopathy assessed by cardiac magnetic resonance. European Heart Journal-Cardiovascular Imaging 16 (1), 29–36.

Arts, T., Hunter, W., Douglas, A., Muijtjens, A., Reneman, R., 1992. Description of the deformation of the left ventricle by a kinematic model. J. Biomech. 25 (10), 1119–1127.

Arvidsson, P.M., Töger, J., Pedrizzetti, G., Heiberg, E., Borgquist, R., Carlsson, M., Arheden, H., 2018. Hemodynamic forces using four-dimensional flow mri: an independent biomarker of cardiac function in heart failure with left ventricular dyssynchrony? American Journal of Physiology-Heart and Circulatory Physiology 315 (6), H1627–H1639.

Baumgartner, H., Falk, V., Bax, J.J., De Bonis, M., Hamm, C., Holm, P.J., Iung, B., Lancellotti, P., Lansac, E., Rodriguez Munoz, D., et al., 2017. 2017 Esc/eacts guidelines for the management of valvular heart disease. Eur. Heart J. 38 (36), 2739–2791.

Baumgartner, H., Stefenelli, T., Niederberger, J., Schima, H., Maurer, G., 1999. Overestimation of catheter gradients by doppler ultrasound in patients with aortic stenosis: a predictable manifestation of pressure recovery. J. Am. Coll. Cardiol. 33 (6), 1655–1661.

Bertoglio, C., Núnez, R., Galarce, F., Nordsletten, D., Osses, A., 2018. Relative pressure estimation from velocity measurements in blood flows: state-of-the-art and new approaches. Int. J. Numer. Method Biomed. Eng. 34 (2), e2925.

Bollache, E., Barker, A.J., Dolan, R.S., Carr, J.C., van Ooij, P., Ahmadian, R., Powell, A., Collins, J.D., Geiger, J., Markl, M., 2018. K-t accelerated aortic 4d flow mri in under two minutes: feasibility and impact of resolution, k-space sampling patterns, and respiratory navigator gating on hemodynamic measurements. Magn. Reson. Med. 79 (1), 195–207.

Bustamante, M., Gupta, V., Forsberg, D., Carlhäll, C.-J., Engvall, J., Ebbers, T., 2018. Automated multi-atlas segmentation of cardiac 4d flow mri. Med. Image Anal. 49, 128–140.

Bustamante, M., Petersson, S., Eriksson, J., Alehagen, U., Dyverfeldt, P., Carlhäll, C.-J., Ebbers, T., 2015. Atlas-based analysis of 4d flow cmr: automated vessel segmentation and flow quantification. Journal of Cardiovascular Magnetic Resonance 17 (1), 87.

Buyens, F., Jolivet, O., De Cesare, A., Bittoun, J., Herment, A., Tasu, J.-P., Mousseaux, E., 2005. Calculation of left ventricle relative pressure distribution in mri using acceleration data. Magnetic Resonance in Medicine: An Official Journal of the International Society for Magnetic Resonance in Medicine 53 (4), 877–884.

Corrado, P.A., Macdonald, J.A., François, C.J., Aggarwal, N.R., Weinsaft, J.W., Wieben, O., 2019. Reduced regional flow in the left ventricle after anterior acute myocardial infarction: a case control study using 4d flow mri. BMC Med. Imaging 19 (1), 101.

Correia, M., Provost, J., Tanter, M., Pernot, M., 2016. 4D ultrafast ultrasound flow imaging: in vivo quantification of arterial volumetric flow rate in a single heartbeat. Physics in Medicine & Biology 61 (23), L48.

Courtois, M., Kovacs, S., Ludbrook, P., 1990. Physiological early diastolic intraventricular pressure gradient is lost during acute myocardial ischemia.. Circulation 81 (5), 1688–1696.

Courtois, M., Kovács Jr, S.J., Ludbrook, P., 1988. Transmitral pressure-flow velocity relation. importance of regional pressure gradients in the left ventricle during diastole.. Circulation 78 (3), 661–671.

De Bruyne, B., Fearon, W.F., Pijls, N.H., Barbato, E., Tonino, P., Piroth, Z., Jagic, N., Mobius-Winckler, S., Rioufol, G., Witt, N., et al., 2014. Fractional flow reserve–guided pci for stable coronary artery disease. N top N. Engl. J. Med. 371 (13), 1208–1217.

Donati, F., Figueroa, C.A., Smith, N.P., Lamata, P., Nordsletten, D.A., 2015. Non-invasive pressure difference estimation from pc-mri using the work-energy equation. Med Image Anal 26 (1), 159–172.

Donati, F., Myerson, S., Bissell, M.M., Smith, N.P., Neubauer, S., Monaghan, M.J., Nordsletten, D.A., Lamata, P., 2017. Beyond bernoulli: improving the accuracy and precision of noninvasive estimation of peak pressure drops. Circulation: Cardiovascular Imaging 10 (1), e005207.

Donati, F., Nordsletten, D.A., Smith, N.P., Lamata, P., 2014. Pressure mapping from flow imaging: enhancing computation of the viscous term through velocity reconstruction in near-wall regions. In: 2014 36th Annual International Conference of the IEEE Engineering in Medicine and Biology Society. IEEE, pp. 5097–5100.

Ebbers, T., Wigström, L., Bolger, A., Wranne, B., Karlsson, M., 2002. Noninvasive measurement of time-varying three-dimensional relative pressure fields within the human heart. J. Biomech. Eng. 124 (3), 288–293.

Ebbers, T., Wigström, L., Bolger, A.F., Engvall, J., Karlsson, M., 2001. Estimation of relative cardiovascular pressures using time-resolved three-dimensional phase contrast mri. Magnetic Resonance in Medicine: An Official Journal of the International Society for Magnetic Resonance in Medicine 45 (5), 872–879.

Eriksson, J., Bolger, A.F., Carlhäll, C.-J., Ebbers, T., 2015. Spatial heterogeneity of four-dimensional relative pressure fields in the human left ventricle. Magn. Reson. Med. 74 (6), 1716–1725.

Eriksson, J., Bolger, A.F., Ebbers, T., Carlhäll, C.-J., 2013. Four-dimensional blood flow-specific markers of lv dysfunction in dilated cardiomyopathy. European Heart Journal–Cardiovascular Imaging 14 (5), 417–424.

Feldman, T., Guerrero, M., 2016. Invasive hemodynamic versus doppler echocardiographic assessment of aortic stenosis severity. Catheter Cardiovasc Interv 87 (3), 498–499.

Ferdian, E., Suinesiaputra, A., Dubowitz, D.J., Zhao, D., Wang, A., Cowan, B., Young, A.A., 2020. 4Dflownet: super-resolution 4d flow mri using deep learning and computational fluid dynamics. Front. Phys. 8, 138.

Firstenberg, M.S., Greenberg, N.L., Garcia, M.J., Thomas, J.D., 2008. Relationship between ventricular contractility and early diastolic intraventricular pressure gradients: a diastolic link to systolic function. Journal of the American Society of Echocardiography 21 (5), 501–506.

Firstenberg, M.S., Smedira, N.G., Greenberg, N.L., Prior, D.L., McCarthy, P.M., Garcia, M.J., Thomas, J.D., 2001. Relationship between early diastolic intraventricular pressure gradients, an index of elastic recoil, and improvements in systolic and diastolic function. Circulation 104 (suppl_1), I–330.

Firstenberg, M.S., Vandervoort, P.M., Greenberg, N.L., Smedira, N.G., McCarthy, P.M., Garcia, M.J., Thomas, J.D., 2000. Noninvasive estimation of transmitral pressure drop across the normal mitral valve in humans: importance of convective and inertial forces during left ventricular filling. J. Am. Coll. Cardiol. 36 (6), 1942–1949.

Fisher, D.C., Tunick, P.A., Kronzon, I., 1998. Large gradient across a partially ligated left atrial appendage. Journal of the American Society of Echocardiography 11 (12), 1163–1165.

Garcia, D., Dumesnil, J.G., Durand, L.-G., Kadem, L., Pibarot, P., 2003. Discrepancies between catheter and doppler estimates of valve effective orifice area can be predicted from the pressure recovery phenomenon: practical implications with regard to quantification of aortic stenosis severity. J. Am. Coll. Cardiol. 41 (3), 435–442.

van der Geest, R.J., Garg, P., 2016. Advanced analysis techniques for intra-cardiac flow evaluation from 4d flow mri. Curr Radiol Rep 4 (7), 38.

Gersh, B.J., Maron, B.J., Bonow, R.O., Dearani, J.A., Fifer, M.A., Link, M.S., Naidu, S.S., Nishimura, R.A., Ommen, S.R., Rakowski, H., et al., 2011. 2011 Accf/aha guideline for the diagnosis and treatment of hypertrophic cardiomyopathy: executive summary: a report of the american college of cardiology foundation/american heart association task force on practice guidelines developed in collaboration with the american association for thoracic surgery, american society of echocardiography, american society of nuclear cardiology, heart failure society of america, heart rhythm society, society for cardiovascular angiography and interventions, and society of thoracic surgeons. J. Am. Coll. Cardiol. 58 (25), 2703–2738.

Geske, J.B., Cullen, M.W., Sorajja, P., Ommen, S.R., Nishimura, R.A., 2012. Assessment of left ventricular outflow gradient: hypertrophic cardiomyopathy versus aortic valvular stenosis. JACC: Cardiovascular interventions 5 (6), 675–681.

Giese, D., Wong, J., Greil, G.F., Buehrer, M., Schaeffter, T., Kozerke, S., 2014. Towards highly accelerated cartesian time-resolved 3d flow cardiovascular magnetic resonance in the clinical setting. Journal of Cardiovascular Magnetic Resonance 16 (1), 42.

Goar, F.G.S., Masuyama, T., Alderman, E.L., Popp, R.L., 1991. Left ventricular diastolic dysfanction in end-stage dilated cardiomyopathy: simultaneous doppler echocardiography and hemodynamic evaluation. Journal of the American Society of Echocardiography 4 (4), 349–360.

Gülan, U., Binter, C., Kozerke, S., Holzner, M., 2017. Shear-scaling-based approach for irreversible energy loss estimation in stenotic aortic flow–an in vitro study. J. Biomech. 56, 89–96.

Haraldsson, H., Kefayati, S., Ahn, S., Dyverfeldt, P., Lantz, J., Karlsson, M., Laub, G., Ebbers, T., Saloner, D., 2018. Assessment of reynolds stress components and turbulent pressure loss using 4d flow mri with extended motion encoding. Magn. Reson. Med. 79 (4), 1962–1971.

Hessenthaler, A., 2020. Multilevel Convergence Analysis: Parallel-in-Time Integration for Fluid-Structure Interaction Problems with Applications in Cardiac Flow Modeling. Institute for Modelling and Simulation of Biomechanical Systems, University of Stuttgart.

Hessenthaler, A., Röhrle, O., Nordsletten, D., 2017. Validation of a non-conforming monolithic fluid-structure interaction method using phase-contrast mri. Int. J. Numer. Method Biomed. Eng. 33 (8), e2845.

Heydari, B., Kwong, R.Y., Jerosch-Herold, M., 2015. Technical advances and clinical applications of quantitative myocardial blood flow imaging with cardiac mri. Prog. Cardiovasc. Dis. 57 (6), 615–622.

Hirt, C.W., Amsden, A.A., Cook, J., 1974. An arbitrary lagrangian-eulerian computing method for all flow speeds. J. Comput. Phys. 14 (3), 227–253.

Hunt, S.A., Baker, D.W., Chin, M.H., Cinquegrani, M.P., Feldman, A.M., Francis, G.S., Ganiats, T.G., Goldstein, S., Gregoratos, G., Jessup, M.L., et al., 2001. Acc/aha guidelines for the evaluation and management of chronic heart failure in the adult: executive summary: a report of the american college of cardiology/american heart association task force on practice guidelines (committee to revise the 1995 guidelines for the evaluation and management of heart failure) developed in collaboration with the international society for heart and lung transplantation endorsed by the heart failure society of america. J. Am. Coll. Cardiol. 38 (7), 2101–2113.

Jain, S., Londono, F.J., Segers, P., Gillebert, T.C., De Buyzere, M., Chirinos, J.A., 2016. Mri assessment of diastolic and systolic intraventricular pressure gradients in heart failure. Curr. Heart Fail. Rep. 13 (1), 37–46.

Jung, B., Stalder, A.F., Bauer, S., Markl, M., 2011. On the undersampling strategies to accelerate time-resolved 3d imaging using k-t-grappa. Magn. Reson. Med. 66 (4), 966–975.

Khalafvand, S., Ng, E., Zhong, L., 2011. Cfd simulation of flow through heart: a perspective review. Comput. Methods Biomech. Biomed. Engin. 14 (01), 113–132.

Londono-Hoyos, F., Segers, P., Hashmath, Z., Oldland, G., Koppula, M.R., Javaid, K., Miller, R., Bhuva, R., Vasim, I., Tariq, A., et al., 2019. Non-invasive intraventricular pressure differences estimated with cardiac mri in subjects without heart failure and with heart failure with reduced and preserved ejection fraction. Open Heart 6 (2), e001088.

Markl, M., Frydrychowicz, A., Kozerke, S., Hope, M., Wieben, O., 2012. 4D flow mri. J. Magn. Reson. Imaging 36 (5), 1015–1036.

Marlevi, D., Ha, H., Dillon-Murphy, D., Fernandes, J.F., Fovargue, D., Colarieti–Tosti, M., Larsson, M., Lamata, P., Figueroa, C.A., Ebbers, T., et al., 2020. Non-invasive estimation of relative pressure in turbulent flow using virtual work-energy. Med. Image Anal. 60, 101627.

Marlevi, D., Ruijsink, B., Balmus, M., Dillon-Murphy, D., Fovargue, D., Pushparajah, K., Bertoglio, C., Colarieti-Tosti, M., Larsson, M., Lamata, P., et al., 2019. Estimation of cardiovascular relative pressure using virtual work-energy. Sci. Rep. 9 (1), 1375.

Pasipoularides, A., Murgo, J.P., Miller, J.W., Craig, W.E., 1987. Nonobstructive left ventricular ejection pressure gradients in man.. Circ. Res. 61 (2), 220–227.

Pedersen, M.M., Pihl, M.J., Haugaard, P., Hansen, K.L., Lange, T., Lönn, L., Nielsen, M.B., Jensen, J.A., 2014. Novel flow quantification of the carotid bulb and the common carotid artery with vector flow ultrasound. Ultrasound in medicine & biology 40 (11), 2700–2706.

Pedrizzetti, G., La Canna, G., Alfieri, O., Tonti, G., 2014. The vortex an early predictor of cardiovascular outcome? Nat. Rev. Cardiol. 11 (9), 545.

Petitjean, C., Dacher, J.-N., 2011. A review of segmentation methods in short axis cardiac mr images. Med. Image Anal. 15 (2), 169–184.

Richter, Y., Edelman, E.R., 2006. Cardiology is flow.

Rovner, A., Greenberg, N.L., Thomas, J.D., Garcia, M.J., 2005. Relationship of diastolic intraventricular pressure gradients and aerobic capacity in patients with diastolic heart failure. American Journal of Physiology-Heart and Circulatory Physiology 289 (5), H2081–H2088.

Schannwell, C.M., Zimmermann, T., Schneppenheim, M., Plehn, G., Marx, R., Strauer, B.E., 2002. Left ventricular hypertrophy and diastolic dysfunction in healthy pregnant women. Cardiology 97 (2), 73–78.

Segletes, S.B., Walters, W.P., 2002. A note on the application of the extended bernoulli equation. Int. J. Impact Eng. 27 (5), 561–576.

Shahcheraghi, N., Dwyer, H., Cheer, A., Barakat, A., Rutaganira, T., 2002. Unsteady and three-dimensional simulation of blood flow in the human aortic arch. J. Biomech. Eng. 124 (4), 378–387.

Sigwart, U., 1995. Non-surgical myocardial reduction for hypertrophic obstructive cardiomyopathy. The Lancet 346 (8969), 211–214.

Stamm, R.B., Martin, R.P., 1983. Quantification of pressure gradients across stenotic valves by doppler ultrasound. J. Am. Coll. Cardiol. 2 (4), 707–718.

Stankovic, Z., Allen, B.D., Garcia, J., Jarvis, K.B., Markl, M., 2014. 4D flow imaging with mri. Cardiovasc. Diagn. Ther. 4 (2), 173.

Thompson, R.B., McVeigh, E.R., 2003. Fast measurement of intracardiac pressure differences with 2d breath-hold phase-contrast mri. Magnetic Resonance in Medicine: An Official Journal of the International Society for Magnetic Resonance in Medicine 49 (6), 1056–1066.

Töger, J., Kanski, M., Carlsson, M., Kovács, S.J., Söderlind, G., Arheden, H., Heiberg, E., 2012. Vortex ring formation in the left ventricle of the heart: analysis by 4d flow mri and lagrangian coherent structures. Ann. Biomed. Eng. 40 (12), 2652–2662.

Van Ooij, P., Allen, B.D., Contaldi, C., Garcia, J., Collins, J., Carr, J., Choudhury, L., Bonow, R.O., Barker, A.J., Markl, M., 2016. 4D flow mri and t1-mapping: assessment of altered cardiac hemodynamics and extracellular volume fraction in hypertrophic cardiomyopathy. J. Magn. Reson. Imaging 43 (1), 107–114.

Vasanawala, S.S., Hanneman, K., Alley, M.T., Hsiao, A., 2015. Congenital heart disease assessment with 4d flow mri. J. Magn. Reson. Imaging 42 (4), 870–886.

Vitiello, R., McCrindle, B.W., Nykanen, D., Freedom, R.M., Benson, L.N., 1998. Complications associated with pediatric cardiac catheterization. J. Am. Coll. Cardiol. 32 (5), 1433–1440.

Wigen, M.S., Fadnes, S., Rodriguez-Molares, A., Bjåstad, T., Eriksen, M., Stensæth, K.H., Støylen, A., Lovstakken, L., 2018. 4-D intracardiac ultrasound vector flow imaging–feasibility and comparison to phase-contrast mri. IEEE Trans. Med. Imaging 37 (12), 2619–2629.

Wyman, R.M., Safian, R.D., Portway, V., Skillman, J.J., McKAY, R.G., Baim, D.S., 1988. Current complications of diagnostic and therapeutic cardiac catheterization. J. Am. Coll. Cardiol. 12 (6), 1400–1406.

Yotti, R., Bermejo, J., Antoranz, J.C., Desco, M.M., Cortina, C., Rojo-Álvarez, J.L., Allué, C., Martín, L., Moreno, M., Serrano, J.A., et al., 2005. A noninvasive method for assessing impaired diastolic suction in patients with dilated cardiomyopathy. Circulation 112 (19), 2921–2929.

Yotti, R., Bermejo, J., Antoranz, J.C., Rojo-Álvarez, J.L., Allue, C., Silva, J., Desco, M.M., Moreno, M., Garcıa-Fernández, M.A., 2004. Noninvasive assessment of ejection intraventricular pressure gradients. J. Am. Coll. Cardiol. 43 (9), 1654–1662.

Zajac, J., Eriksson, J., Dyverfeldt, P., Bolger, A.F., Ebbers, T., Carlhäll, C.-J., 2015. Turbulent kinetic energy in normal and myopathic left ventricles. J. Magn. Reson. Imaging 41 (4), 1021–1029.

Zotti, C., Luo, Z., Lalande, A., Jodoin, P.-M., 2018. Convolutional neural network with shape prior applied to cardiac mri segmentation. IEEE J Biomed Health Inform 23 (3), 1119–1128.